



# Interfacial delivery of carbon monoxide via smart titanium implant coating for enhanced soft tissue integration with switchable antibacterial and immunomodulatory properties

Minghao Zhou<sup>a,1</sup>, Gangfeng Li<sup>b,1</sup>, Jingwei Yu<sup>a,1</sup>, Qian Zhou<sup>b</sup>, Kun Wang<sup>b</sup>, Jiaxin Kang<sup>a</sup>, Tengjiao Wang<sup>b,c,d,\*\*</sup>, Peng Li<sup>b,c,\*</sup>, Hongbo Wei<sup>a,\*\*\*</sup>

<sup>a</sup> State Key Laboratory of Oral & Maxillofacial Reconstruction and Regeneration, National Clinical Research Center for Oral Diseases, Shaanxi Engineering Research Center for Dental Materials and Advanced Manufacture, Department of Oral Implants, School of Stomatology, The Fourth Military Medical University, Xi'an, Shaanxi, PR China

<sup>b</sup> Frontiers Science Center for Flexible Electronics (FSCFE), Institute of Flexible Electronics (IFE) & Institute of Biomedical Materials and Engineering (IBME), Northwestern Polytechnical University (NPU), Xi'an, Shaanxi, PR China

<sup>c</sup> School of Flexible Electronics, Henan Institute of Flexible Electronics (HIFE), Henan University, 379 Mingli Road, Zhengzhou, 450046, PR China

<sup>d</sup> Chongqing Innovation Center, Northwestern Polytechnical University, Chongqing, 401135, PR China

## ARTICLE INFO

### Keywords:

Gastrotransmitters  
Soft tissue integration  
Immune microenvironment  
Ti implants  
Antibacterial

## ABSTRACT

Soft tissue integration around titanium (Ti) implants is weaker than that around natural teeth, compromising long-term success of Ti implants. Carbon monoxide (CO) possesses distinctive therapeutic properties, rendering it as a highly promising candidate for enhancing STI. However, achieving controlled CO generation at the STI interface remains challenging. Herein, a controlled CO-releasing dual-function coating was constructed on Ti surfaces. Under near-infrared (NIR) irradiation, the designed surface could actively accelerate CO generation for antibiosis against both aerobic and anaerobic bacteria. More importantly, in the absence of NIR, the slow release of CO induces macrophage polarization from pro-inflammatory phenotype towards pro-regenerative phenotype. In a rat implantation model with induced infection, the designed surface effectively controlled the bacterial infection, alleviates accompanying inflammation and modulated immune microenvironment, leading to enhanced STI. Single-cell sequencing revealed that the coating alters the cytokine profile within the soft tissue, thereby influencing cellular functions. Differentially expressed genes in macrophages are highly enriched in the PI3K-Akt pathway. Furthermore, the cellular communication between fibroblasts and macrophages was significantly enhanced through the CXCL12/CXCL14/CXCR4 and CSF1-CSF1R ligand-receptor pair. These findings indicate that our coating showed an appealing prospect for enhancing STI around Ti implants, which would ultimately contribute to the improved long-term success of Ti implants.

Peer review under responsibility of KeAi Communications Co., Ltd.

\* Corresponding author. Frontiers Science Center for Flexible Electronics (FSCFE), Institute of Flexible Electronics (IFE) & Institute of Biomedical Materials and Engineering (IBME), Northwestern Polytechnical University (NPU), Xi'an, Shaanxi, PR China.

\*\* Corresponding author. Frontiers Science Center for Flexible Electronics (FSCFE), Institute of Flexible Electronics (IFE) & Institute of Biomedical Materials and Engineering (IBME), Northwestern Polytechnical University (NPU), Xi'an, Shaanxi, PR China.

\*\*\* Corresponding author. State Key Laboratory of Oral & Maxillofacial Reconstruction and Regeneration, National Clinical Research Center for Oral Diseases, Shaanxi Engineering Research Center for Dental Materials and Advanced Manufacture, Department of Oral Implants, School of Stomatology, The Fourth Military Medical University, Xi'an, Shaanxi, PR China.

E-mail addresses: [iamtjwang@nwpu.edu.cn](mailto:iamtjwang@nwpu.edu.cn) (T. Wang), [iamppli@nwpu.edu.cn](mailto:iamppli@nwpu.edu.cn) (P. Li), [weihongbo@fmmu.edu.cn](mailto:weihongbo@fmmu.edu.cn) (H. Wei).

<sup>1</sup> These authors contributed equally to this work.

<https://doi.org/10.1016/j.bioactmat.2024.06.010>

Received 19 March 2024; Received in revised form 17 May 2024; Accepted 6 June 2024

2452-199X/© 2024 The Authors. Publishing services by Elsevier B.V. on behalf of KeAi Communications Co. Ltd. This is an open access article under the CC BY-NC-ND license (<http://creativecommons.org/licenses/by-nc-nd/4.0/>).

## 1. Introduction

Peri-implant soft-tissue integration (STI) serves as a critical barrier against the invasion from the external environment, and is essential for long-term implant success [1,2]. Nevertheless, compared to natural teeth, the STI around Ti implants exhibits substantially weaker attachment and heightened susceptibility to disruption. This difference is likely attributed to the bio-inert nature of Ti surface, which limits protein adsorption and hinders robust tissue integration [3]. Breaching this transmucosal barrier triggers a cascade of adverse biological complications, including peri-implant mucosal inflammation, bone resorption, and ultimately, implant failure [4]. Studies report a considerable range in the incidence of peri-implant mucositis (40–65 %), peri-implantitis (20–47 %), and implant failure (3–10 %) [5]. These complications exact a significant toll on patient well-being and healthcare systems, with estimated annual costs exceeding \$1 billion in the United States [6]. In fact, the surgical implantation of Ti implants inevitably induce the activation of the host's immune response, fostering an environment that is susceptible to infection [7]. This inflammatory milieu attracts and concentrates implant pathogens associated with implant infection, as well as immune cells in the soft tissue around implant, leading to concerted metabolic activity that alters the surrounding immune-microenvironment [8]. The altered immune-microenvironment, characterized by elevated pro-inflammatory cytokines and diminished phagocytic activity, orchestrates a transition to chronic inflammation, further jeopardizing stable STI formation through a vicious cycle of tissue destruction [8,9]. Therefore, modulating the local immune-microenvironment around the interface between the Ti implant and soft tissue to enhance STI holds great potentials for the success of Ti implants.

Macrophages play a crucial role in immunomodulation orchestrating the dynamic process of STI. The equilibrium between tissue breakdown and repair is governed by their phenotype transitions between the pro-inflammatory M1 phenotype and the pro-regenerative M2 phenotype.<sup>10</sup>,<sup>11</sup> Macrophages undergo a phenotypic transformation during STI, shifting the functional state in response to the changing tissue environment [10,11]. The formation and maintenance of STI is facilitated by the immune-microenvironment created by M2 macrophages, which secrete a range of tissue regenerative cytokines and anti-inflammatory factors [9,12]. However, in the pathological state of infection, the dysfunctional macrophages exhibit an inability to effectively undergo a phenotype transition from M1 to M2 status. Therefore, it is crucial to suppress excessive inflammatory response and timely trigger macrophage polarization from M1 to M2 phenotype. A number of bioactive immunomodulators, such as cytokines [13], inflammatory mediator [14], enzymes [15], and genes [16] have been identified as effective tools for modulating immune response. For instance, Ballestas et al. reported the delivery of FTY720, an immunomodulatory drug, promotes oral wound healing by inducing a pro-regenerative immune response with increased M2 macrophages [17]. However, the shortcomings including difficulties in delivery, slow effect, high cost, and additional antibiotic needed in the infectious environment remain to be resolved [17,18]. Hence, it is important for STI enhancement to develop an active immune regulation method at the STI interface to induce macrophage polarization towards a pro-regenerative phenotype.

Carbon monoxide (CO), one of the gasotransmitters, is increasingly appreciated as a crucial endogenous signaling molecules and has been confirmed to possess prominent immunomodulation and antibacterial effects. CO exerts anti-inflammatory effects through inhibition of various pro-inflammatory cytokines and activating the heme oxygenase-1 (HO-1) to block a variety of pro-inflammatory signaling pathways, such as mitogen-activated protein kinase and nuclear factor kappa B [19,20]. What's more, CO could induce the polarization of macrophages from M1 towards M2 phenotype through the JAK-STAT6 pathway, promoting a shift from pro-inflammatory to pro-regenerative response. Zhang et al. developed a CO prodrug-loaded mesoporous polydopamine nanoparticles coated by chitosan/alginate polyelectrolytes, which could

ameliorate inflammation and manifest an immunomodulatory effect through CO-driven macrophage polarization towards M2 phenotype [21]. When the equilibrium of host immunity is disrupted (e.g. implant surgery) creating a susceptible environment, on-demand CO release at high concentrations exhibits excellent antibacterial properties through mechanisms such as bacterial membrane permeabilization, disruption of ATP synthesis, and inhibition of cellular respiration [22,23]. The rapid eradication of bacteria by CO contributes to the elimination of inflammation in infected tissues, accelerating the transition from the inflammatory phase to the tissue repair phase. The considerable benefits of CO-based therapy are attributed to its low propensity to develop bacterial resistance, favorable biocompatibility, and protective role in diverse physiological and pathological activities within tissues [24,25]. In consideration of the different roles that CO plays in bacteria and living tissues, it is a promising strategy to enhance STI by controlling local CO generation at the STI interface to realize the functional switch between immunomodulation and antibiosis.

Herein, a controlled CO-releasing dual-function coating on Ti surfaces was constructed. As illustrated in Fig. 1, assisted by the mild hyperthermia induced by NIR irradiation, the coating was triggered on-demand release of a large amount of CO for bacterial killing in susceptible environment. The CO release was 12.4-fold higher at 30 min after NIR irradiation compared to non-irradiated controls. The antibacterial experiment revealed that post-NIR irradiation, the coating exhibited a strong antibacterial effect with *S. aureus* and *P. gingivalis*. More importantly, after bacterial elimination, the coating could spontaneously generate CO in a sustained way, alleviating inflammatory response by inhibiting various pro-inflammatory cytokines secretion from M1 macrophages. Additionally, it could further induce the macrophage polarization from pro-inflammatory M1-phenotype to pro-regenerative M2-phenotype, remodeling the impaired immune-microenvironment into a pro-regenerative state, which is beneficial for STI improvement. The *in vivo* evaluation indicated the improved epithelial integrity, augmented collagen synthesis, and enhanced expression of integrin- $\beta$ 4 and laminin- $\beta$ 3 at the STI interface. Ultimately, single-cell sequencing highlighted the coating's role in shaping the immune microenvironment around implants. The coating altered the cytokine profile within the soft tissue, potentially affecting cellular behavior of macrophages and fibroblasts. Notably, fibroblasts-macrophage crosstalk was significantly augmented through the CXCL12/CXCL14/CXCR4 and CSF1-CSF1R. Taken together, the interfacial strategy proposed in this work enables a functional switch between immunomodulation and antibiosis by actively regulating CO release, thereby promoting STI around Ti implants.

## 2. Results and discussion

### 2.1. Fabrication and characterization of Ti-DOPA-CO

A peptidomimetic functional coating with abundant catechols and thiol groups was developed by the co-deposition of levodopa (*L*-DOPA) and pentaerythritol tetraenyl (3-mercaptopropionic acid) (PETMP); followed by coupling with thermosensitive CO releasing molecules (CORMs), triiron dodecacarbonyl ( $\text{Fe}_3(\text{CO})_{12}$ ). Multivalent catecholic molecules facilitate facile and enduring binding onto various materials via mussel-inspired molecular adhesion [26]. The thiol-reactive surface exhibits excellent biological activity, promoting cell attachment and alignment [27–29]. Additionally, immobilization of thermosensitive CORMs onto the coating through the coupling with excess thiol groups could achieve localized and controlled CO release properties. As illustrated in Fig. 2A, polished Ti substrate were first treated by oxygen plasma, which could produce a surface activation reaction with hydroxyl groups. The *L*-DOPA and PETMP were then co-deposited on Ti surfaces in Tris buffer for 48 h. The catechol groups in *L*-DOPA adhere to activated Ti surface via hydrogen bonds, and the thiol groups in PETMP were cross-linked to *L*-DOPA via Michael addition to form a non-linear film. Co-deposition of *L*-DOPA and PETMP showed a gradual increase

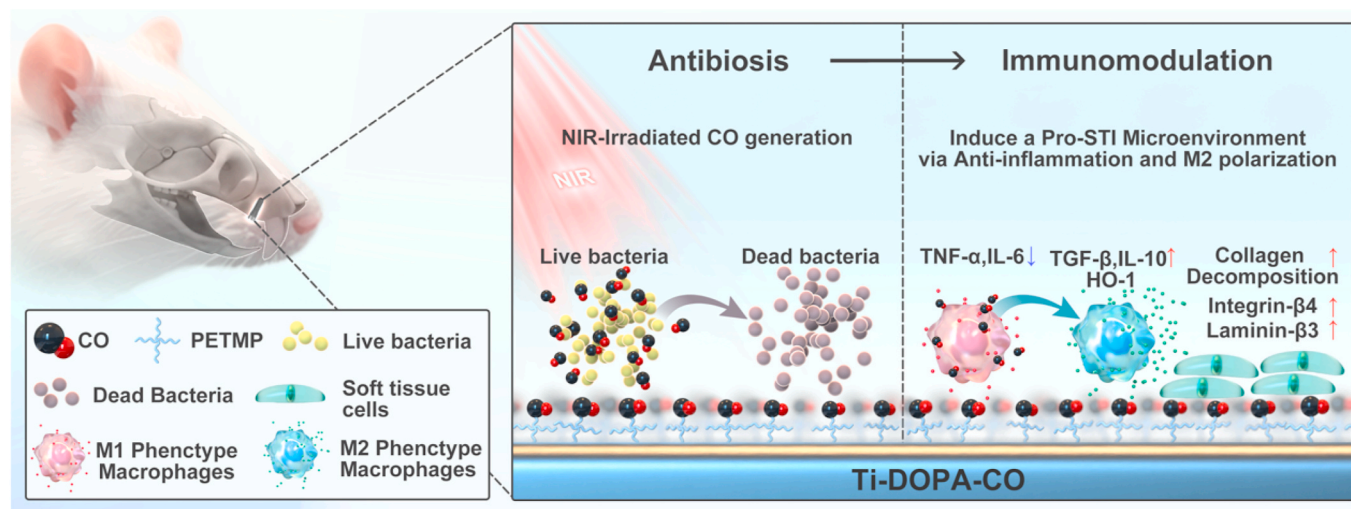


Fig. 1. Schematic illustration of Ti-DOPA-CO implant for STI enhancement through CO-mediated immunomodulation and antibiosis.

in thickness from 6 to 48 h (6, 12, 24, 48 h), reaching a maximum of  $32 \pm 1.6$  nm. However, at 72 h, a decrease and inconsistent thickness measurements were observed, indicating instability (Fig. S1). Therefore, 48 h emerged as the ideal co-deposition time for maximizing consistent coating thickness, denoted as Ti-DOPA.  $\text{Fe}_3(\text{CO})_{12}$ , a typical thermosensitive CORMs, were finally coupled with unreacted thiol groups to achieve surface immobilization. Seeking an effective balance between high CORMs loading and minimal impact on biocompatibility, substrates prepared with different concentrations of CORMs were screened through *in vitro* Alamar Blue assay. The substrates immobilized with CORMs at concentration of 1, 3, 5 mg/mL maintained good biocompatibility in comparison to Ti and Ti-DOPA. However, when the concentration increased to 8 and 10 mg/mL, the substrates exhibited a notable reduction biocompatibility (Fig. S2). Consequently, 5 mg/mL was selected as the concentrations of CORMs to prepare the final substrates, denoted as Ti-DOPA-CO.

After the key parameter for coating preparation were established, the surface properties of the samples were characterized. SEM was utilized to observe the surface morphology of various substrates (Fig. 2B). The pure Ti displayed relatively smooth surface with some minor grooves related to the polishing with carbide sandpaper. After introducing the L-DOPA onto the Ti substrate, the minor grooves disappeared, and a uniform coating was formed. The immobilization of CORMs resulted in a relatively rough and amorphous surface morphology. Furthermore, the arithmetic mean surface roughness (Ra) was determined from the AFM topographic images (Fig. 2C). The pure Ti substrate and Ti-DOPA-CO showed relatively smooth surface morphology with an Ra value of  $19.76 \pm 2.12$  nm, while the surface roughness of Ti-DOPA-CO significantly increased with an Ra value of  $30.04 \pm 2.54$  nm (Fig. S3). After  $\text{Fe}_3(\text{CO})_{12}$  deposition, the roughness of the modified surface slightly increased, as indicated by the Ra value of  $33.48 \pm 3.79$  nm (Fig. S3). In addition to surface roughness, the surface wettability was further determined by water contact angle measurement. As shown in Fig. S4, the water contact angle of Ti substrates was  $79.80 \pm 2.48^\circ$ , indicating weak hydrophilicity. However, the water contact angle of Ti-DOPA decreased to  $22.47 \pm 3.03^\circ$ , which could be attributed to the high hydrophilicity of L-DOPA. After the immobilization of CORMs, the water contact angle of Ti-DOPA-CO increased to  $41.47 \pm 6.60^\circ$ . The possible explanation is that the surface energy decreases to reduce the system's energy during the deposition and drying process. Overall, the results of water contact measurement indicated that Ti-DOPA and Ti-DOPA-CO substrates were more hydrophilic than the pure Ti substrate. XPS was used to characterize the surface chemical compositions of the different substrate (Fig. S5). Compared to the Ti, the signal of N 1s and S 2p were

detected in Ti-DOPA, and N 1s, S 2p, and Fe 2p were detected in Ti-DOPA-CO. The above results demonstrated that Ti-DOPA-CO was successfully developed. The adhesion strength of the coating was assessed utilizing the nanoscratch test [30,31]. The critical load ( $L_c$ ) is defined as the force at which a sudden change in the load force is detected, serving as an indicator of the coating's adhesion strength to the substrate [31, 32]. As marked in Fig. S6, an abrupt change in the load force was observed at around 30 s, indicating an alteration of the contact surface against the diamond indenter. This shift is indicative of a transition between the coating and the substrate, with the  $L_c$  value approximating 150.0 mN. Measurements were replicated at three different random sites on each specimen, calculating the adhesion strength of Ti-DOPA-CO to be approximately  $166 \pm 34$  mN. It should be noted that multiple factors could influence the results of scratch test, including loading rate, scratching speed, indenter tip radius, substrate and coating properties, and surface roughness, etc. [30] Therefore, comparisons of  $L_c$  value can be only in the case when influencing factors remain constant.

The on-demand release of CO plays a crucial role in diverse biological functions, including efficient transitions between bacterial eradication and subsequent M2 macrophage polarization for tissue repair. This research delves into this understudied area by demonstrating that Ti-DOPA-CO regulate this switch through its NIR-triggered rapid CO release and sustained release profile without NIR irradiation, potentially unveiling a promising strategy for STI enhancement. As shown in Fig. S7, the temperature of Ti-DOPA-CO in PBS displayed a power-intensity-dependent manner. After 10 min of NIR irradiation, the surface temperature of the Ti-DOPA-CO substrate gradually rose to 26.8, 32.0, 37.1, 42.5, 46.3 °C with power density of 0.4, 0.6, 0.8, 1.0, and 1.2  $\text{W}/\text{cm}^2$ , respectively. Studies have shown that the cellular contents such as protein and DNA would be damaged when the local temperature exceeds 43 °C [33]. To avoid the potential thermal injury to normal cells or tissues, 1.0  $\text{W}/\text{cm}^2$  was selected as the power density for subsequent experiments. Real-time thermographic images revealed that the surface temperature of Ti-DOPA-CO increased from 22 °C to 29.8, 35.4, 39.5, 42.5 °C after NIR irradiation (1.0  $\text{W}/\text{cm}^2$ ) of 100, 200, 300, and 600 s (Fig. 2D). Additionally, the photothermal conversion of Ti-DOPA-CO was maintained across three on/off cycles of NIR irradiation, indicating its photothermal stability and recyclability (Fig. S8). The NIR laser, serving as a convenient and controllable exogenous stimulus, finds extensive application in inducing photothermal therapy (PTT) and photodynamic therapy (PDT) to achieve antibacterial and antitumor effects [34–36]. Additionally, it functions as an external switch to activate drug release from hydrogels and nanomaterials, thereby promoting wound healing [34,37].  $\text{Fe}_3(\text{CO})_{12}$ , a well-characterized thermosensitive

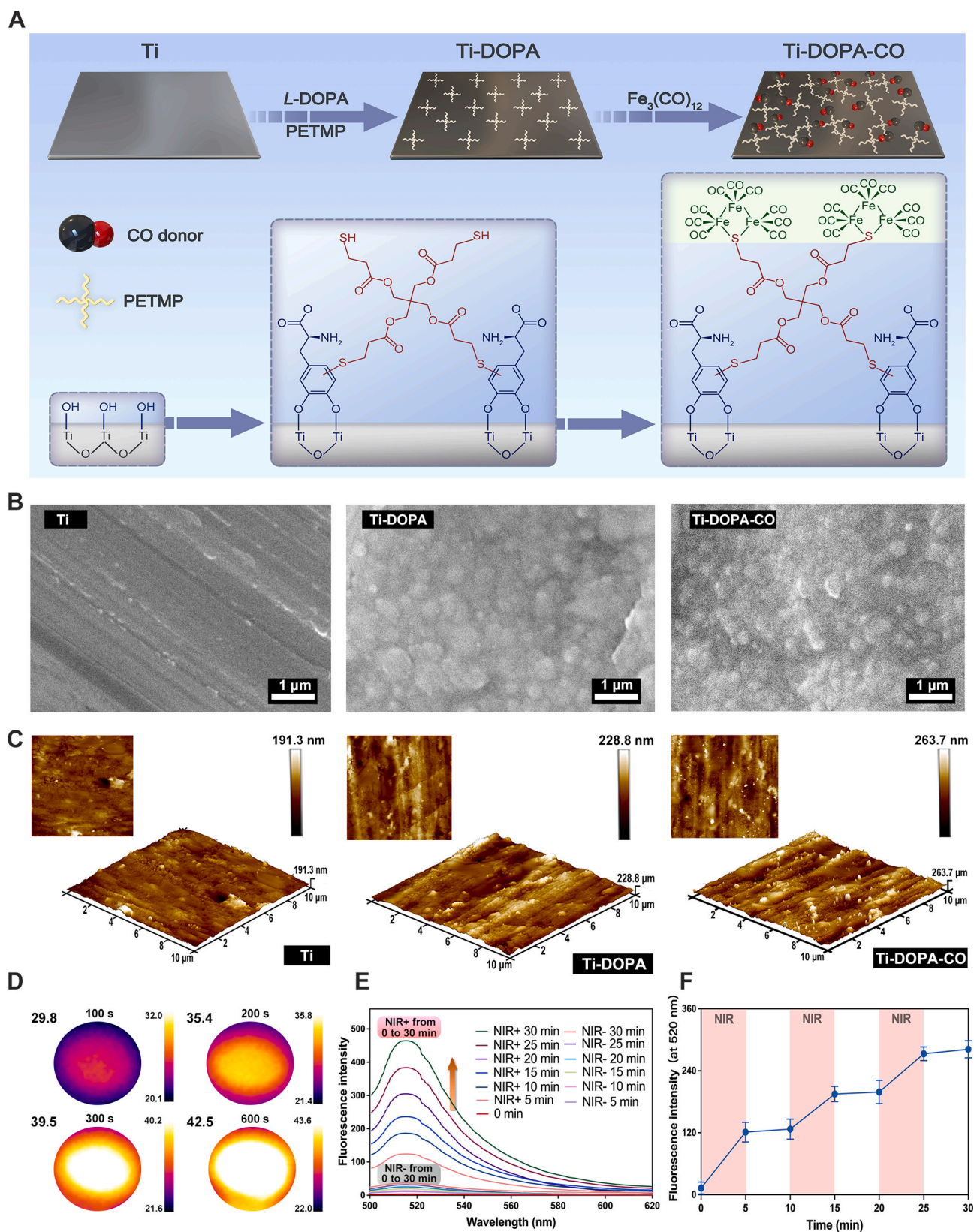


**Fig. 2.** Fabrication and characterization of Ti-DOPA-CO. A) Schematic illustration for the preparation of peptidomimetic functional CO releasing coating. B) Representative SEM images of Ti, Ti-DOPA, and Ti-DOPA-CO. C) AFM analysis on Ti, Ti-DOPA, and Ti-DOPA-CO with  $10 \times 10 \mu\text{m}^2$  section. D) Real-time thermographic images of Ti-DOPA-CO under NIR irradiation ( $1.0 \text{ W/cm}^2$ ). E) Fluorescent spectra for CO release of Ti-DOPA-CO in PBS with or without NIR irradiation ( $1.0 \text{ W/cm}^2$ ) measured using CO probe system (FL-CO-1 +  $\text{PdCl}_2$ ,  $5 \mu\text{M}$  each). The spectra were recorded every 5 min. F) CO release behavior from Ti-DOPA-CO triggered by NIR laser ( $1.0 \text{ W/cm}^2$ ) switch on and off repeated three times. Data are presented as mean  $\pm$  S.D. ( $n = 3$ ).

CORMs, releases CO slowly through hydrolysis under normal conditions, but increased temperature, often mediated by photothermal effect, significantly accelerate hydrolysis and thus trigger rapid CO release [38]. In this study, NIR was utilized to induce rapid CO release. By harnessing the photothermal properties of Ti-DOPA-CO and the thermosensitive  $\text{Fe}_3(\text{CO})_{12}$ , the NIR laser initiated a local thermal effect, thus facilitating the rapid release of CO from Ti-DOPA-CO. The impact of temperature changes alone on the CO release from Ti-DOPA-CO was firstly examined. The results indicated that at room temperature, the release of CO was slow and minimal. However, when the temperature was elevated and sustained at 42.5 °C, there was a marked acceleration in CO release (Fig. S9). The photothermal effect of Ti-DOPA-CO could raise the surface temperature upon NIR irradiation, thereby inducing active NIR-triggered CO release through the same accelerated hydrolysis mechanism. A reported CO-responsive fluorescent probe (FL-CO-1) system was used to monitor the CO generation of Ti-DOPA-CO [19]. Despite its non-fluorescent nature, this probe system unveils an effective approach for CO detection by exhibiting a prompt fluorescent response for CO in the presence of  $\text{PdCl}_2$ , enabling rapid and sensitive fluorescent measurements [39]. As displayed in Fig. 2E, Ti-DOPA-CO showed distinct fluorescence enhancement after continuous NIR irradiation for 30 min, demonstrating effective CO generation upon NIR irradiation. While the fluorescence intensity only slightly increased without NIR irradiation during the same period, indicating a very small amount of CO release from Ti-DOPA-CO. The CO release was then calculated according to the standard curve (Fig. S10). The results showed that, following 30 min of NIR irradiation, the CO release was 12.4 times that of the non-irradiated control groups (Fig. S11). Furthermore, the on-demand CO release from Ti-DOPA-CO was investigated under intermittent NIR irradiation. As shown in Fig. 2F, after NIR irradiation for 5 min, a rapid release of CO was detected. When the NIR was switched off, CO release almost stopped. The above-mentioned results indicated that Ti-DOPA-CO could generate CO in response to NIR stimulation and the CO release could be tailored with intermittent NIR irradiation.

The final products following CO release under NIR irradiation were determined by EDS, XPS, and ICP-OES. The EDS mapping exhibited that elements of Fe, S, and O was distributed on the surface of Ti-DOPA-CO after NIR irradiation (Fig. S12). Furthermore, the high-resolution XPS survey scan were performed to confirm the presence of a mixed valence state of Fe ( $\text{Fe}^{2+}$  and  $\text{Fe}^{3+}$ ) (Fig. S13). The findings from EDS and XPS measurements imply that subsequent to NIR irradiation, Fe is likely immobilized on the substrate surface in a mixed state, consisting of a mixture of iron oxides, iron sulfides, and organic compounds. However, as one of the essential elements for the human body, iron play a crucial role in various biological effects in living systems, such as cellular respiration, oxygen storage, and energy metabolism [40]. Therefore, the concentration of released iron was quantified using the ICP-OES after Ti-DOPA-CO was irradiated by NIR. The results indicated that only extremely small amount iron was released with a concentration of  $0.079 \pm 0.008$  ppm on the day 7 after NIR irradiation (Fig. S14). This concentration is much lower than the concentration (50–500  $\mu\text{g}/\text{mL}$ ) at which iron ions exert biological effects in local tissues [41–44]. Therefore, in this study, we primarily focus on the biological effects of CO released from Ti-DOPA-CO.

## 2.2. *In vitro* antibacterial activity

The aerobic *Staphylococcus aureus* (*S. aureus*) and the anaerobic *Porphyromonas gingivalis* (*P. gingivalis*) were selected to assess the antibacterial properties since they are two major pathogenic bacteria associated with peri-implant infections [45,46]. Firstly, the plate coating method was utilized to evaluate the *in vitro* antibacterial properties of Ti-DOPA-CO against *S. aureus* and *P. gingivalis* was investigated (Fig. 3A–D). As shown in Fig. 3A and C Ti-DOPA exhibited almost no antibacterial ability against *S. aureus* and *P. gingivalis*, with or without NIR irradiation. Similarly, Ti-DOPA-CO had an inconspicuous

bactericidal activity without NIR stimulation, indicating a compromised bactericidal effect under low amount of CO generation. However, after NIR irradiation (1  $\text{W}/\text{cm}^2$ ) for 10 min, the number of bacteria on the Ti-DOPA-CO was significantly reduced with a survival rate of  $12.3 \pm 5.3$  % for *S. aureus* and  $9.1 \pm 3.4$  % for *P. gingivalis* (Fig. 3B and D). Furthermore, Live/Dead fluorescent staining was carried out to monitor the viability of bacterial populations of different groups (Fig. 3E). Compared with Ti, Ti + NIR, and Ti-DOPA, tiny amounts of dead bacteria were observed for Ti-DOPA + NIR and Ti-DOPA-CO, demonstrating their inadequate antibacterial ability of single hyperthermia or low amount of CO release. In a stark contrast, most of the *S. aureus* and *P. gingivalis* on the Ti-DOPA-CO + NIR are stained fluorescent red, suggesting that they are dead with damaged membranes. Additionally, SEM was used to observe the morphological changes of bacteria on the various substrates (Fig. 3F). Both *S. aureus* and *P. gingivalis* on Ti-DOPA-CO + NIR group exhibited considerable shrinkage or membrane rupture, while of bacteria on the other groups maintained an intact morphology with smooth surfaces. These results suggest that Ti-DOPA-CO has a significant bactericidal effect against both *S. aureus* and *P. gingivalis*, primarily due to the rapid release of CO induced by NIR irradiation.

It is reported that Ru-based CORMs, including CORM-2 and CORM-3, the antibacterial effect could largely be attributed to the chemical reactivity of ruthenium [47,48]. Despite its thermosensitive properties,  $\text{Fe}_3(\text{CO})_{12}$  was selected as the CORM to develop the coating in this study is attributed to its outstanding biosafety when considering the metal metabolites among various carbonyl complexes of transition metals, as iron is one of the trace elements in the human body [49,50]. The concentration of released iron was quantified using the ICP-OES after Ti-DOPA-CO was irradiated by NIR. The results indicated that only extremely small amount iron was released with a concentration of  $0.079 \pm 0.008$  ppm on the day 7 after NIR irradiation (Fig. S14). This concentration is significantly lower than the threshold at which iron ions cause cytotoxicity and exert their antibacterial effects [51,52].

## 2.3. *In vitro* immunomodulation evaluation

Prior to assessing the *in vitro* immunomodulatory efficacy of Ti-DOPA-CO, an evaluation of its cytocompatibility towards macrophages was conducted. Minimal cell death was observed across all substrates, thereby substantiating the cytocompatibility of Ti-DOPA-CO with macrophages (Fig. S15A). In addition, the result of the Alamar-Blue assay indicated that there was no significant disparity in cell viability observed on each set of substrates, which further confirms the cytocompatibility of Ti-DOPA-CO (Fig. S15B). Research has substantiated significant contributions of macrophages in the dynamic process of STI [12,53]. Initially, these cells undergo polarization into the pro-inflammatory M1 phenotype, to engage in immune activation, subsequently transitioning into the pro-regenerative M2 phenotype to participate in STI [9]. Nevertheless, in the infectious microenvironment, dysfunctional macrophages encounter difficulties in smoothly transitioning from M1 to M2 phenotype due to the excessive presence of pro-inflammatory cytokines. Consequently, various substrates were co-incubated with lipopolysaccharide (LPS)-stimulate macrophages (M1 phenotype) to simulate the switch in macrophage phenotype under the infectious microenvironment (Fig. 4A). The immunofluorescence staining of the markers for macrophages (M1: CD86, M2: CD 206) was performed. As shown in Fig. 4B and C, immunofluorescence staining for CD86 exhibited positive results in macrophages that were stimulated by LPS, while staining against CD206 predominantly showed negative results. No discernible differences in the expression of CD86 or CD206 were detected among the LPS, Ti, and Ti-DOPA groups. In sharp contrast, macrophages in the Ti-DOPA-CO group exhibited a discernibly diminished CD86 signal and an enhanced CD206 signal. These results suggest that Ti-DOPA-CO exerts immunomodulatory effects that suppress M1 polarization while promoting activating transformation of

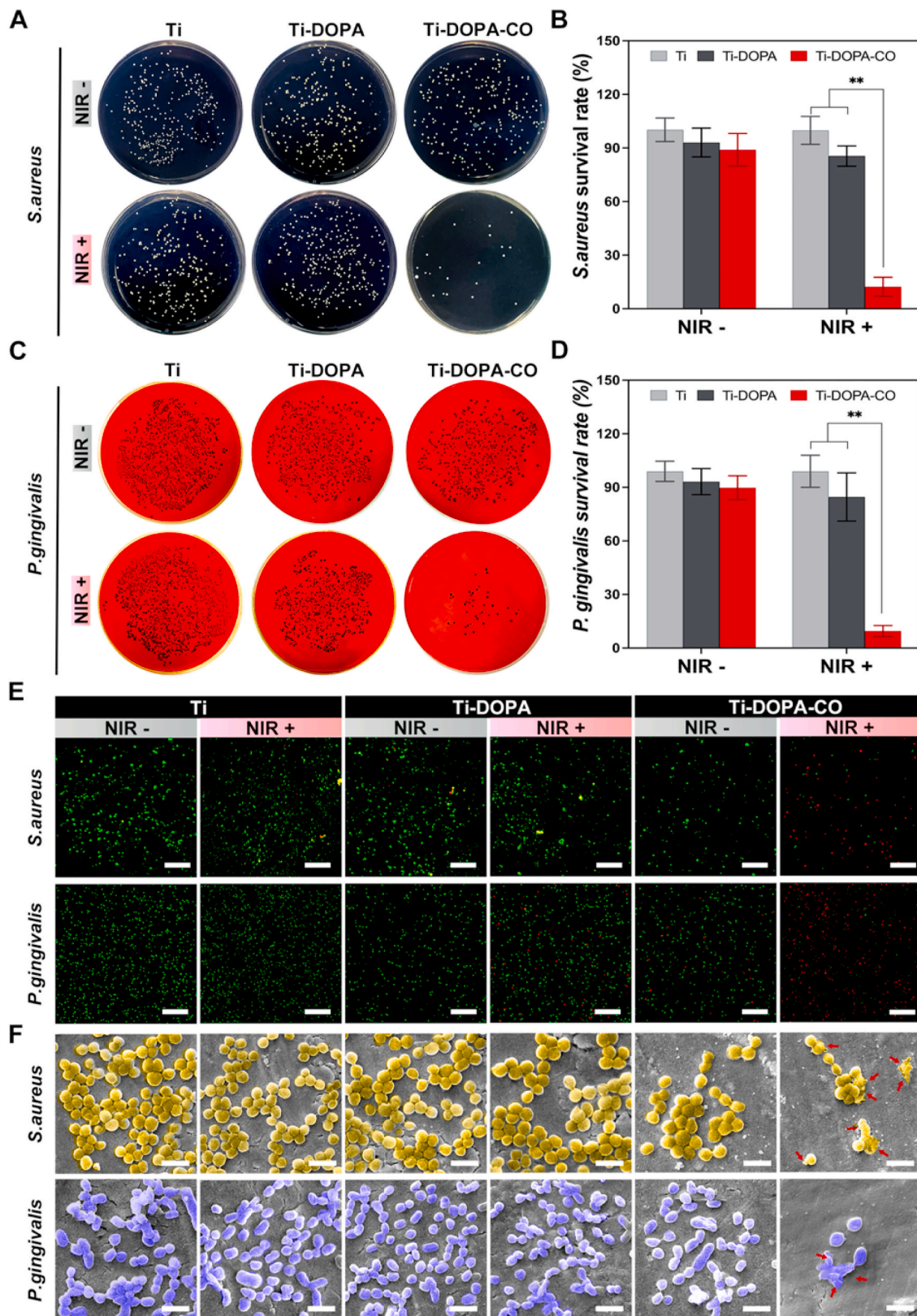


**Fig. 3.** *In vitro* antibacterial properties against *S. aureus* and *P. gingivalis*. A) Images of the bacterial colonies formed by *S. aureus* cultures in different groups with or without NIR irradiation and B) corresponding survival rate of *S. aureus*. C) Images of the bacterial colonies formed by *P. gingivalis* cultures in different groups with or without NIR irradiation and D) corresponding survival rate of *P. gingivalis*. E) Fluorescent images exhibiting the Live/Dead distribution of *S. aureus* and *P. gingivalis* on surfaces of different substrates (scale bar = 100 μm). F) SEM images of *S. aureus* and *P. gingivalis* on the surfaces of different substrates (scale bar = 1 μm). Data are presented as mean ± S.D. (n = 3; \*\*p < 0.01). Fluorescent staining and SEM were repeated three time independently, yielding the similar results.

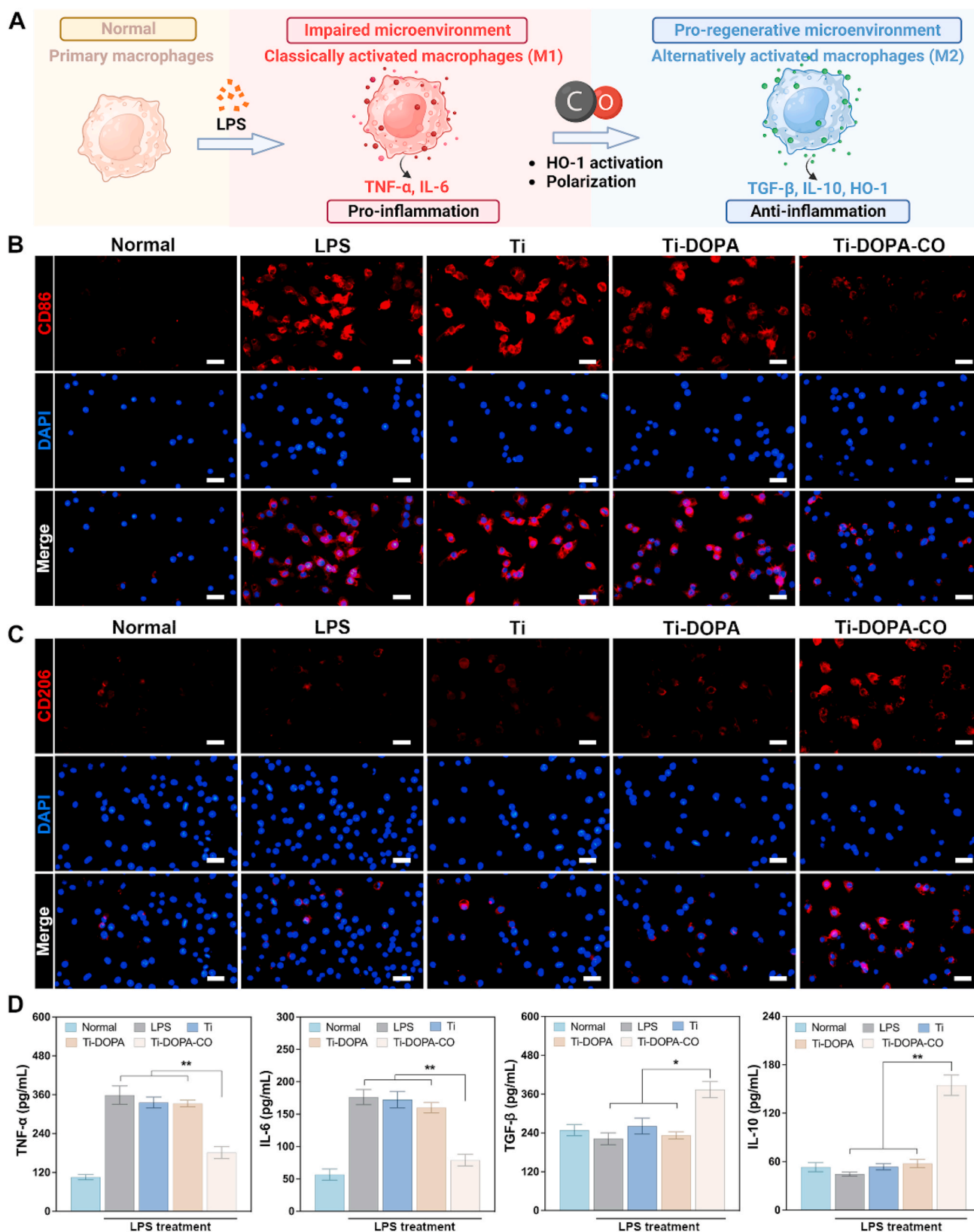


**Fig. 4.** *In vitro* anti-inflammation and immunomodulation ability A) Schematic illustration of anti-inflammation and immunomodulation by NIR-triggered CO generation. B, C) Fluorescent staining images of marker of RAW264.7 after different treatment (red: CD86 or CD206, blue: nuclei; scale bar = 20  $\mu$ m). D) ELISA analysis of pro-inflammatory cytokines (TNF- $\alpha$  and IL-6) and anti-inflammatory cytokines (TGF- $\beta$  and IL-10) secreted by normal and LPS-induced macrophages after different treatment. Data are presented as mean  $\pm$  S.D. (n = 3; \*p < 0.05 and \*\*p < 0.01). Fluorescent staining was repeated three time independently, yielding the similar results.

macrophages toward the M2 phenotype. Similarly, the rapid CO release from Ti-DOPA-CO induced by NIR irradiation also promoted the polarization of LPS-treated macrophages to M2 phenotype (Fig. S16). The prevailing understanding is that persistent oxidative stress serves as a

primary catalyst for inflammation, whereas CO has the capability of counteracting oxidative stress through the activation of heme oxygenase (HO-1), consequently impeding the inflammation [54,55]. It is also reported that the macrophages reprogramming effect of CO is associated

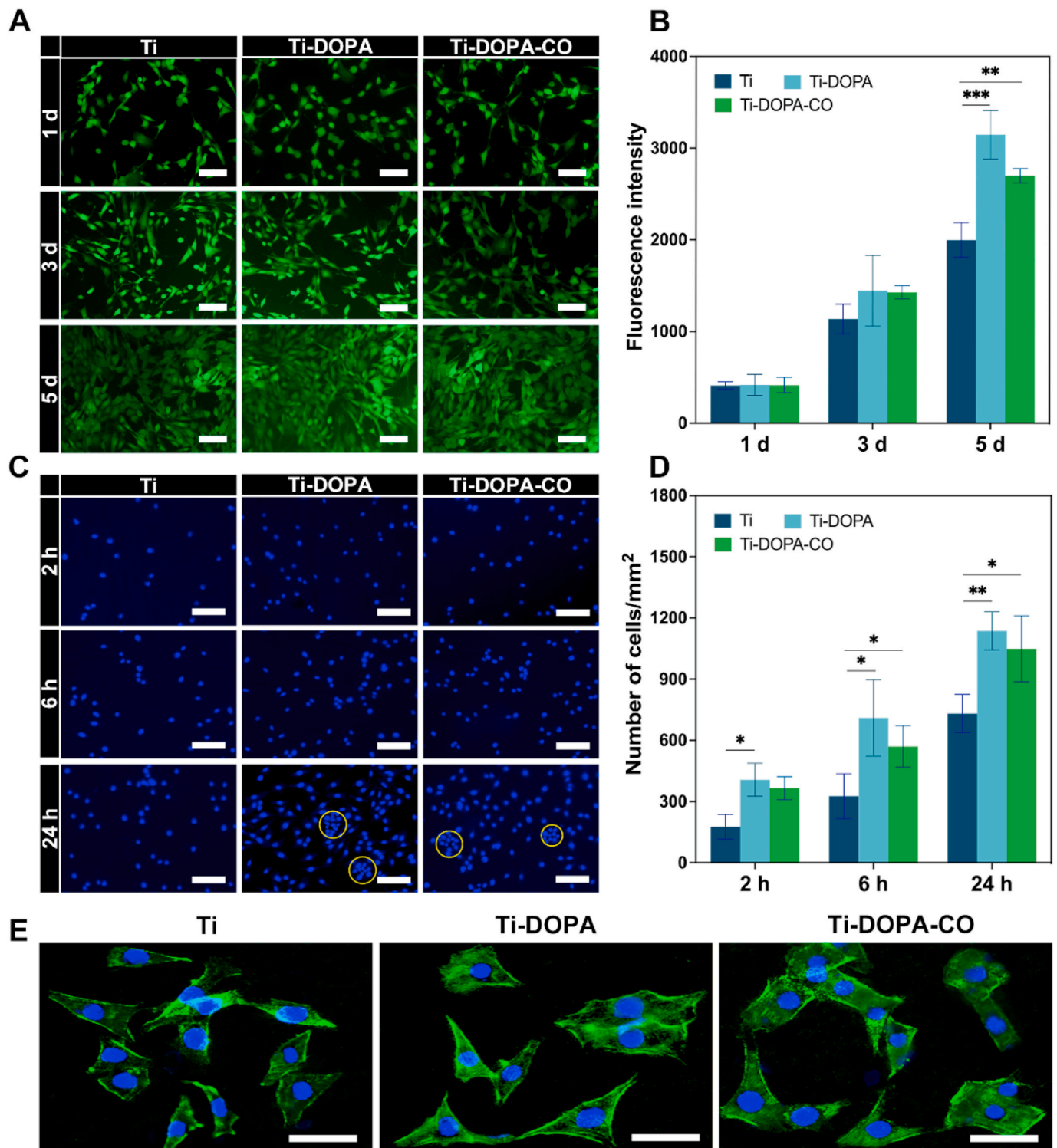


**Fig. 5.** Cellular behavior of fibroblasts on Ti-DOPA-CO. A) Live/Dead staining images of NIH3T3 on different substrates at days 1, 3, and 5 (scale bar = 100  $\mu$ m). B) Fluorescent intensity of Alamar Blue assay showing the cell viability of NIH3T3 at days 1, 3, and 5. C) Immunofluorescence staining of 4,6-diamidino-2-phenylindole (DAPI) after NIH3T3 were cultures on different substrates for 2, 6, and 24 h (scale bar = 100  $\mu$ m). Yellow cycle showing the cells reaching confluency. D) Quantitative analysis for cell number seeded on different substrates at 2, 6, and 24 h. E) The actin cytoskeleton of NIH3T3 cultured on various substrates for 24 h was visualized by phalloidin-FITC (green) staining (scale bar = 50  $\mu$ m). Immunofluorescence staining was repeated three time independently, yielding similar results. Data are presented as mean  $\pm$  S.D. (n = 3; \*p < 0.05, \*\*p < 0.01, and \*\*\*p < 0.001).

with positive induction of HO-1 [56]. As shown in Fig. S17, the expression of HO-1 was notably increased in the macrophages after treatment with Ti-DOPA-CO, aligning with previous studies [54]. Furthermore, in order to assess the anti-inflammatory capabilities, an enzyme-linked immunosorbent assay (ELISA) was conducted to measure the levels of excretive pro-inflammatory (TNF- $\alpha$ , IL-6) and anti-inflammatory (IL-10, TGF- $\beta$ ) cytokines. As shown in Fig. 4D, the levels of TNF- $\alpha$  and IL-6 were significantly decreased in the Ti-DOPA-CO group in comparison to Ti-DOPA group. Conversely, the levels of TGF- $\beta$  and IL-10 were increased, indicating the anti-inflammatory capabilities of Ti-DOPA-CO.

#### 2.4. *In vitro* cell Behavioral experiment

It is widely recognized that biocompatibility is a fundamental requirement for implanted biomaterials and optimal implants should exhibit a favorable response towards the soft tissue cells [53]. A comprehensive evaluation of fibroblast cellular behavior on Ti-DOPA-CO was performed, including cytocompatibility, cell proliferation, adhesion, and morphology. Firstly, the cytocompatibility of various substrates was evaluated by Live/Dead staining and Alamar-Blue assay. As shown in Fig. 5A, all substrates displayed good cytocompatibility with negligible numbers of dead found on their surfaces after 1, 3, and 5 days of incubation, indicating that the immobilization of Fe<sub>3</sub>(CO)<sub>12</sub> and subsequent release of a low-dose of CO had no pronounced cytotoxic effect on NIH3T3. The results were further supported by the cell proliferation measurements using Alamar-blue assay (Fig. 5B). Cell proliferation levels of all groups increased over incubation time. No significant difference was found in day 1 and 3, but the cell cultured on Ti-DOPA and Ti-DOPA-CO showed a stronger proliferation by day 5 compared with pure Ti. Additionally, the cell viability was evaluated to determine whether the NIR triggered CO release has a negative impact of BMSCs and NIH3T3. After 10 min of NIR irradiation, no significant differences in cell viability were observed for both BMSCs and NIH3T3 cells cultured with Ti-DOPA-CO, suggesting that the rapid release of CO from Ti-DOPA-CO had no negative impact on cell viability (Fig. S18). However, in a separate study, BMSCs exhibited significantly reduced cell viability on the designed surface following 10 min of NIR-triggered CO release, which could be attributed to higher CO concentrations and temperatures compared to those in this study [56]. The adhesion of NIH3T3 was subsequently determined. Immunofluorescence staining showed that cells cultured Ti-DOPA and Ti-DOPA-CO had a higher cell density compared with that on pure Ti after 2, 4, and 6 h of incubation (Fig. 5C and D). After 24 h of incubation, cells cultured on Ti-DOPA and Ti-DOPA-CO exhibited increased density and displayed aggregation, whereas cells on the pure Ti substrate remained dispersed and showed less confluency. Furthermore, cellular morphology and spreading were observed with cytoskeleton staining. Fig. 5E shows that NIH3T3 interacted strongly with all the substrates after 24 h of incubation. In contrast to the pure Ti group, NIH3T3 cultured on Ti-DOPA and Ti-DOPA-CO substrates exhibited a greater presence of contractile stress fibers and more pronounced cell body spreading. The results above demonstrate that Ti-DOPA-CO not only possesses favorable biocompatibility but also support fibroblast proliferation and adhesion. These beneficial outcomes are likely to confer advantages for the *in vivo* STI formation.

#### 2.5. *In vivo* antibiosis and immunomodulation

Following the positive *in vitro* results, a comprehensive series of *in vivo* experiments were undertaken to evaluate the efficacy of Ti-DOPA-CO, which included assessments of its antibacterial properties, immunomodulatory effects, and STI performance. A rat maxillary implantation model with an induced infectious microenvironment was prepared for *in vivo* experiments. The timeline of the *in vivo* experiment is depicted in Fig. 6A. The process of model construction is depicted in Fig. S19. One

month after tooth extraction, various implants were inserted into the maxillary, followed by the inoculation with an *S. aureus* suspension. Subsequently, the implants were subjected to NIR irradiation for three days. To assess the antibacterial effects of implants in each group, the soft tissue around implant was harvested on day 4 to quantify the bacterial colonies (Fig. 6B and C). Both Ti-DOPA + NIR and Ti-DOPA-CO groups showed limited antibacterial effects with an antibacterial rate of  $17.3 \pm 4.5\%$  and  $21.3 \pm 6.1\%$ , respectively. Distinctly, the Ti-DOPA-CO + NIR group displayed better antibacterial efficiency with an antibacterial rate of  $90.3 \pm 5.6\%$ . These results were consistent with the *in vitro* experiments and indicated that the enhanced antibacterial effect was due to the NIR-irradiated CO release from Ti-DOPA-CO. Collectively, NIR-triggered antibiosis from Ti-DOPA-CO was confirmed in the implantation model with induced infectious microenvironment, which is a necessary condition for subsequent processes such as anti-inflammatory, immunomodulation, and STI formation.

After resolving a bacterial infection environment, the peri-implant soft tissue enters a repair and regeneration stage, ultimately establishing STI with the implant surface. Our coating could release CO in a sustained way without NIR, affecting the immune response by mitigating inflammation and promoting M2 macrophage polarization, thus creating a favorable immune-microenvironment for enhanced STI. Relative mRNA expression levels of the marker of M1 (iNOS and CD86) and M2 (Arg-1 and CD206) macrophages in peri-implant soft tissue were detected by q-PCR. It was found that the expression levels of iNOS and CD86 were highest in soft tissue surrounding the Ti-DOPA-CO implant, while the levels of Arg-1 and CD206 were lower than those of the other groups (Fig. 6D). In addition, the double immunofluorescence staining with F4/80 and iNOS (M1 marker) or Arg-1 (M2 marker) was performed, respectively (Fig. 6E and F). In Ti-DOPA-CO group, there was significant reduction in the distribution of iNOS positive macrophages, while a predominantly stronger trend was observed in Arg-1 positive macrophages. Quantitative analysis showed a significant decrease in the ratio of iNOS<sup>+</sup> in F4/80<sup>+</sup> macrophages compared to the other groups (Fig. 6G). In contrast, a higher proportion of Arg-1<sup>+</sup> expression was observed in F4/80<sup>+</sup> macrophages compared to the remaining groups (Fig. 6H).

As revealed by Hematoxylin and Eosin (H&E) staining, significant inflammatory infiltration and collagen damage in connective tissue were observed in Ti and Ti-DOPA groups. Conversely, attenuated inflammation and well-organized collagen was observed in soft tissue around Ti-DOPA-CO (Fig. S20). Additionally, the levels of pro-inflammatory (TNF- $\alpha$  and IL-6) and anti-inflammatory (IL-10 and TGF- $\beta$ ) cytokines were detected in the peri-implant soft tissue (Fig. 6I). Treatment with Ti-DOPA-CO resulted in a significant reduction in the levels of TNF- $\alpha$  and IL-6 compared to that in Ti and Ti-DOPA, implying a notable attenuation of the inflammation. In contrast, the levels of anti-inflammatory cytokines (IL-10 and TGF- $\beta$ ) in Ti-DOPA-CO implant was statistically higher than that in other groups, suggesting a profound anti-inflammatory effect mediated by CO release from Ti-DOPA-CO.

#### 2.6. *In vivo* osseointegration and STI evaluation

The osseointegration of an implant is critical for its optimal function within the oral cavity during mastication. Accordingly, the osseointegration capabilities of various implants were initially assessed after a 4-week implantation period. Micro-CT images revealed that the implants were accurately positioned in the location of the first maxillary molar and showed successful osseointegration (Fig. 7A). Moreover, quantitative analyses from micro-CT scans indicated no significant differences in bone volume fraction (BV/TV), trabecular thickness (Tb. Th), trabecular number (Tb. N), and trabecular separation (Tb. Sp) across the different groups. This indicates that Ti-DOPA-CO does not compromise osseointegration when compared to pure titanium implants (Fig. 7B–E).

Motivated by the favorable *in vivo* antibacterial and immunomodulatory effects, the STI formation was evaluated at 4-week post-

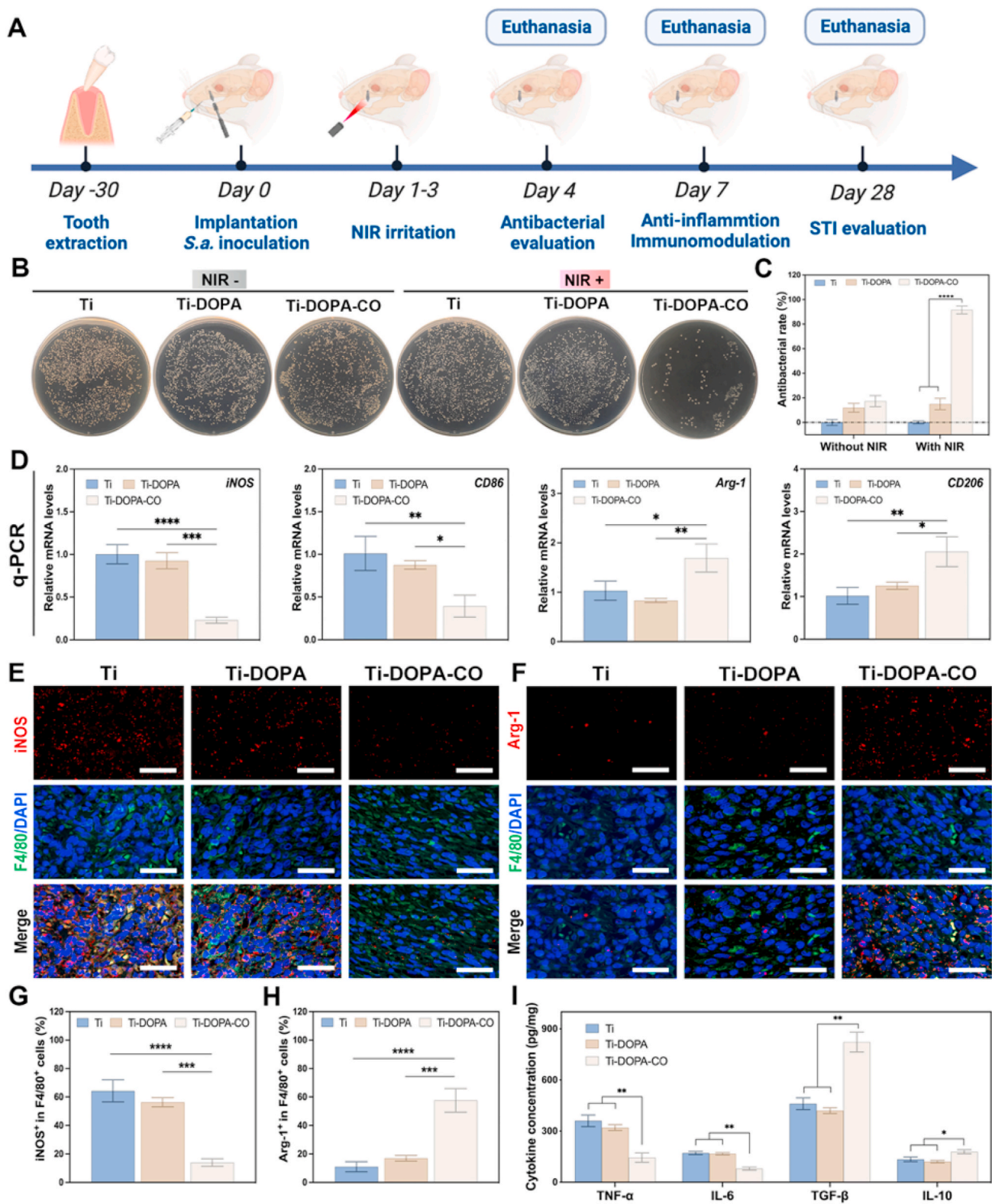


**Fig. 6.** In vivo antibacterial and immunomodulatory properties in an induced infectious model. A) Flow diagram of the *in vivo* experiments. B) *S. aureus* colonies formed on LB solid medium of different groups. C) Quantitative analysis of antibacterial efficacy by counting the colonies in different groups. D) Relative mRNA expression levels of the marker of M1 (iNOS and CD86) and M2 (Arg-1 and CD206) macrophages in soft tissue. E, F) Immunofluorescent staining of F4/80 (macrophage marker) and iNOS (M1 marker) or Arg-1 (M2 marker) in peri-implant soft tissue (scale bar = 50 μm). Semiquantitative analysis of G) iNOS and H) Arg-1 positive area/F4/80 positive area. I) ELISA analysis of pro-inflammatory cytokines (TNF-α and IL-6) and anti-inflammatory cytokines (TGF-β and IL-10) from the peri-implant soft tissue in different groups. Immunofluorescence staining was repeated three time independently, yielding similar results. Data are presented as mean ± S.D. (n = 3; \*p < 0.05, \*\*p < 0.01, \*\*\*p < 0.001, and \*\*\*\*p < 0.0001).

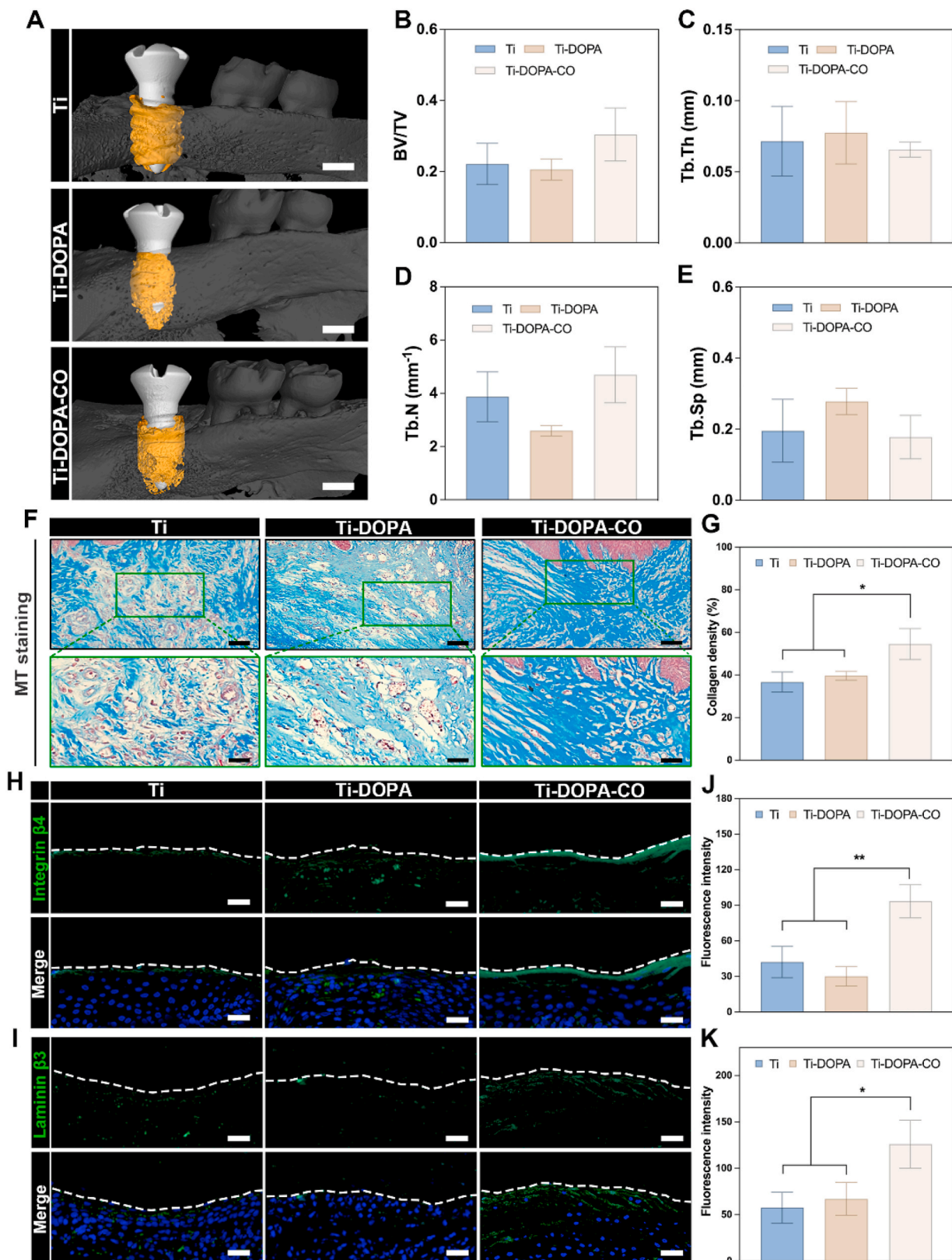


**Fig. 7.** In vivo osseointegration and STI evaluation. A) Micro-CT 3D reconstruction images of the rat maxillary region (including implants; scale bar = 1 mm). B-E) Quantification of BV/TV, Tb.Th, Tb.N, and Tb.Sp from Micro-CT scanning. F) MT staining (upper scale bar = 200 μm, lower scale bar = 50 μm) and G) corresponding quantitative analysis of collagen deposition density. Immunofluorescence staining of H) Integrin β4 and I) Laminin β3 (subunit of laminin 332) in the implant-soft-tissue interface (scale bar = 50 μm) and J, K) corresponding quantitative analysis. MT staining and immunofluorescence staining was repeated three time independently, yielding similar results. Data are presented as mean ± S.D. (n = 3; \*p < 0.05 and \*\*p < 0.01).

implantation. H&E staining indicated that the formation of epithelium was distinct and fully developed in the Ti-DOPA-CO group, characterized by the presence of complete epithelial layers (Fig. S21). In contrast, the remaining groups exhibited thin and interrupted epithelial layers. Subsequently, collagen deposition in the peri-implant connective tissue of the different groups was assessed using the Masson's Trichrome (MT) and Van Gieson (VG) staining (Fig. 7F and Fig. S22A). Abundant collagen deposition and a notable level of directional alignment were observed in the Ti-DOPA-CO group, indicating a positive reconstitution of extracellular matrix and soft tissue remodeling. The findings were further corroborated by the quantitative analysis of collagen deposition density, wherein the Ti-DOPA-CO exhibited the highest collagen deposition density (Fig. 7G and Fig. S22B). Indeed, prior research by Cai et al. yielded analogous findings, demonstrating that the CO release from Fe<sub>3</sub>(CO)<sub>12</sub> exhibits potent bactericidal properties and anti-inflammatory characteristics, ultimately facilitating advantageous soft tissue regeneration [57]. Subsequently, the expression of Integrin  $\beta$ 4 and Laminin  $\beta$ 3 (subunit of laminin 332) at the interface between the implant and soft tissue were detected by immunofluorescence staining (Fig. 7H and I). Compared to the Ti and Ti-DOPA groups, the expression levels of both proteins were significantly higher in the Ti-DOPA-CO group (Fig. 7J and K). Collectively, the *in vivo* findings suggest that under NIR activation, Ti-DOPA-CO initially releases a significant amount of CO, contributing to effective bacterial killing in the infectious microenvironment. Furthermore, the sustained release of CO at lower concentrations demonstrated immunomodulation effects, collectively supporting the STI enhancement.

In summary, our findings suggest that Ti-DOPA-CO positively influences peri-implant STI via antibiosis and immunomodulation. To further understand the immunomodulatory effect of Ti-DOPA-CO on the peri-implant microenvironment, single-cell RNA sequencing (scRNA-seq) was employed to sequence cells from peri-implant soft tissues 28 days post-implantation.

### 2.7. Changes in peri-implant immune microenvironment of Ti-DOPA-CO via scRNA-seq analysis

Fresh peri-implant soft tissue from the Ti and Ti-DOPA-CO groups were collected, then dissected and digested into single cells. The single-cell data are presented into two-dimensional space using the uniform manifold approximation and projection (UMAP) method. The unsupervised clustering was assigned to 7 main classes of cells, including basal cells, endothelial cells, fibroblasts, mural cells, duct cells, T cells, and myeloid cells (macrophages, neutrophils, langerhans cells, conventional dendritic cells) (Fig. 8A). The composition of each cluster is listed to identify the proportion of cells from two groups across all cell clusters. Differential expressed genes (DEGs) for each cell type were computed and the top 3 DEGs were visualized in the dot plot (Fig. 8B).

The cytokine profile in the peri-implant microenvironment around two groups was initially analyzed (Fig. 8C). The results showed a total of 31 differentially expressed cytokines (DECs), among which 23 were expressed at significant higher levels and 8 at significantly lower levels in the Ti-DOPA-CO group compared with Ti group.

Functional enrichment analysis of the DECs showed that, at the biological process level, there was a notable enrichment in cytokine-mediated signaling, myeloid leukocyte migration, and granulocyte and leukocyte chemotaxis (Fig. 8D). At the cellular component level, the DECs were mainly distributed in the external side of plasma membrane and receptor complex. While for molecular function level, DECs associated with cytokine receptor binding, signaling receptor regulator activity, and immune receptor activity were most heavily enriched in. Taken together, these results imply that Ti-DOPA-CO could modulate the cytokine profile in the peri-implant soft tissue microenvironment, which in turn may influence cellular activities. The convergence of our *in vitro* and *in vivo* findings with existing literature consistently points to CO's ability to drive macrophage polarization toward the M2 phenotype

[56,58]. Furthermore, the research by Chen et al. posits that a cytokine milieu associated with the M2 phenotype may be more favorable for STI development [9]. Interestingly, Kyoto Encyclopedia of Genes and Genomes (KEGG) pathway enrichment analysis on DEGs of macrophages between two groups was performed, indicating that DEGs was highly enriched in the PI3K-Akt signaling pathway (Fig. 8E). These results suggest that Ti-DOPA-CO may induce the M2 macrophage polarization via the PI3K-Akt signaling pathway. The research conducted by Cai et al. also provides evidence for this perspective [59]. Subsequently, an analysis of the DEGs within fibroblast was conducted across two sample groups (Fig. 8F). Gene Ontology (GO) enrichment analysis revealed that the DEGs are primarily involved in: extracellular matrix organization, collagen synthesis, cell-substrate junction, and connective tissue development. These functional items are intimately linked to the development of STI, suggesting that Ti-DOPA-CO plays a role in altering the peri-implant immune microenvironment, which in turn augments fibroblast activities pertinent to STI.

### 2.8. Enhanced cellular communication between fibroblasts and macrophages in the peri-implant immune environment

To explore the interaction in both Ti and Ti-DOPA-CO groups between macrophages and fibroblasts within the Ti-DOPA-CO group, CellPhoneDB was utilized to profile the intercellular communication. Strong interactions were observed between macrophages, basal cells, endothelial cells, and fibroblasts (Fig. 9A and B). However, the Ti-DOPA-CO group, there was a significant increase in the interaction between macrophages and fibroblasts compared to the Ti group (Fig. 9C and D). Crucially, analysis of the chemokine ligand-receptor pairs indicated that fibroblast-macrophage communication was significantly enhanced via the CXCL12-CXCR4 and CXCL14-CXCR4 in Ti-DOPA-CO (Fig. 9E). Indeed, targeting CXCL12-CXCR4 axis is a potentially selective method of immunomodulation and activation of CXCR4 leads to macrophage polarization switching from M1 to M2 phenotype [60]. Additionally, in the Ti-DOPA-CO group, another significantly intensified macrophage-fibroblast interaction pair was identified: CSF1-CSFR1 (Fig. 9F). Studies suggest that fibroblasts and macrophages engage in direct interactions centered on the CSF1-CSFR1 axis to influence the overall microenvironment [61]. Fibroblasts can support macrophages in a microenvironment via the provision of CSF1, which can be a signal expression of a macrophage-specific transcriptional program. While macrophages can provide direct signals, such as TGF- $\beta$ , to fibroblasts to promote their proliferation and activation. Overall, the cellular communication analysis suggests that Ti-DOPA-CO facilitates immunomodulation through reciprocal communication between macrophages and fibroblasts via the CXCL12/CXCL14/CXCR4 and CSF1-CSFR1 ligand-receptor pair.

Upon integrating experimental data with single-cell sequencing insights, we propose a possible explanation whereby Ti-DOPA-CO promote peri-implant STI through immunomodulation. The local release of CO from Ti-DOPA-CO exerts an immunomodulatory effect within the peri-implant immune microenvironment by facilitating interactions between fibroblasts and macrophages through the CXCL12/CXCL14/CXCR4 and CSF1-CSFR1 ligand receptor pairs. These interactions contribute to a change in cytokine profiles, characterized by M2 macrophages polarization and fibroblasts activation, thereby fostering an immune microenvironment conducive for STI. It is critical to acknowledge the intricate and nuanced regulation of the peri-implant immune microenvironment during STI development, which involves the interplay of multiple cell types. Therefore, a more comprehensive analysis of the immune cytokine landscape and cellular type is necessitated. Our analysis focuses on macrophages and fibroblasts, the principal cells implicated in STI, to offer a plausible explanation for the role of immunomodulation in STI and provides both experimental evidence and a theoretical foundation for further investigation.

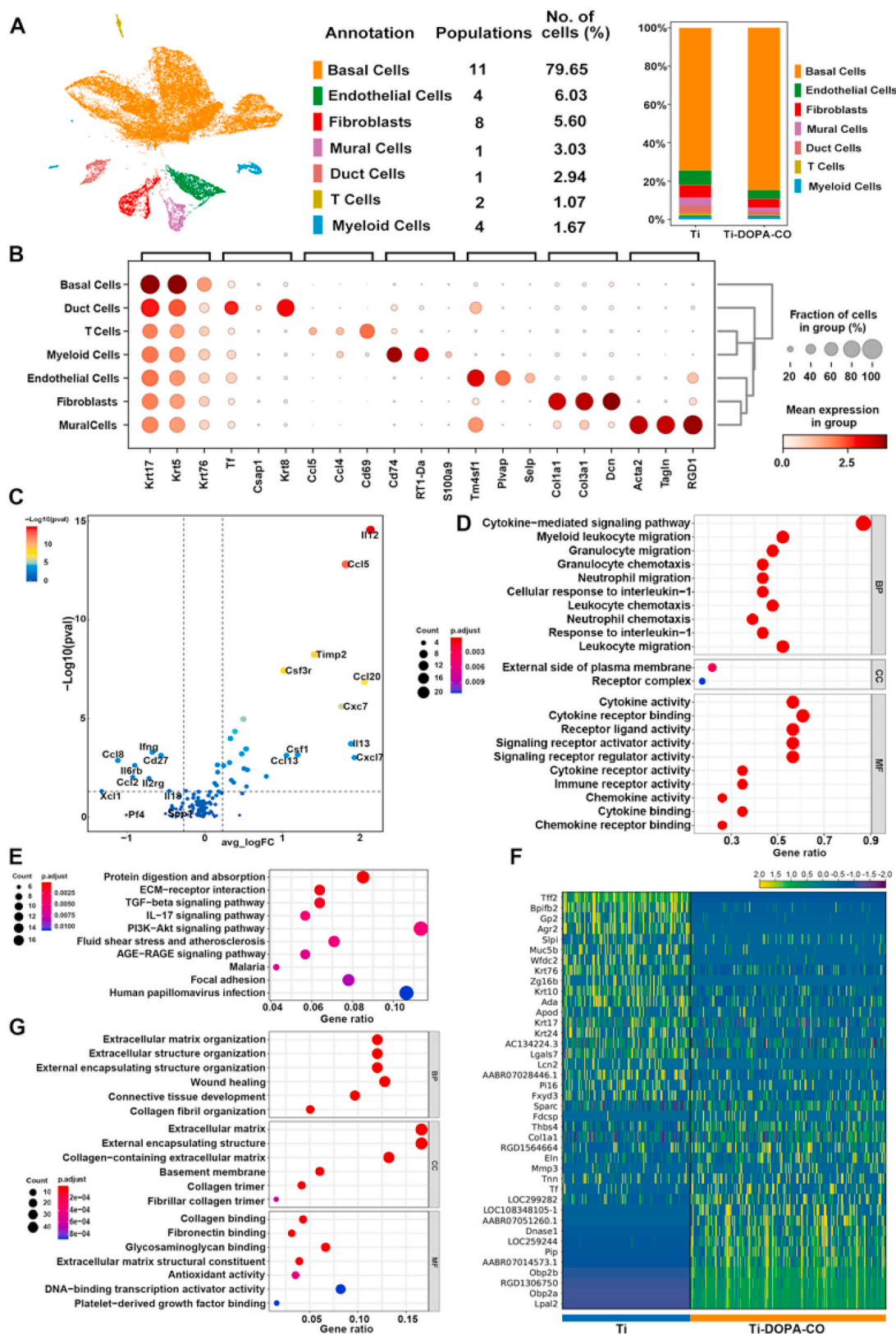


**Fig. 8.** scRNA-Seq analysis revealing the changes in peri-implant immune microenvironment. A) UMAP representation of major cell types identified by scRNA-seq (n = 3; left). Cell population, number of cells (%), and composition of Ti and Ti-DOPA-CO cells are listed. Bar plots indicating the percentage of cell types in Ti and Ti-DOPA-CO groups (right). B) Dot plot showing the top three marker genes for each cell types. C) Volcano plot depicting DECs between Ti and Ti-DOPA-CO groups. D) GO analysis revealing the top terms enriched in biological process (BP), cellular component (CC), and molecular function (MF) for DECs between Ti and Ti-DOPA-CO groups. E) KEGG analysis indicating the top ten signaling pathway enriched in DEGs of macrophages between Ti and Ti-DOPA-CO groups. F) Heat map showing DEGs of fibroblasts between Ti and Ti-DOPA-CO groups. G) GO analysis revealing the top terms enriched in BP, CC, and MF for DEGs in fibroblasts between Ti and Ti-DOPA-CO groups.

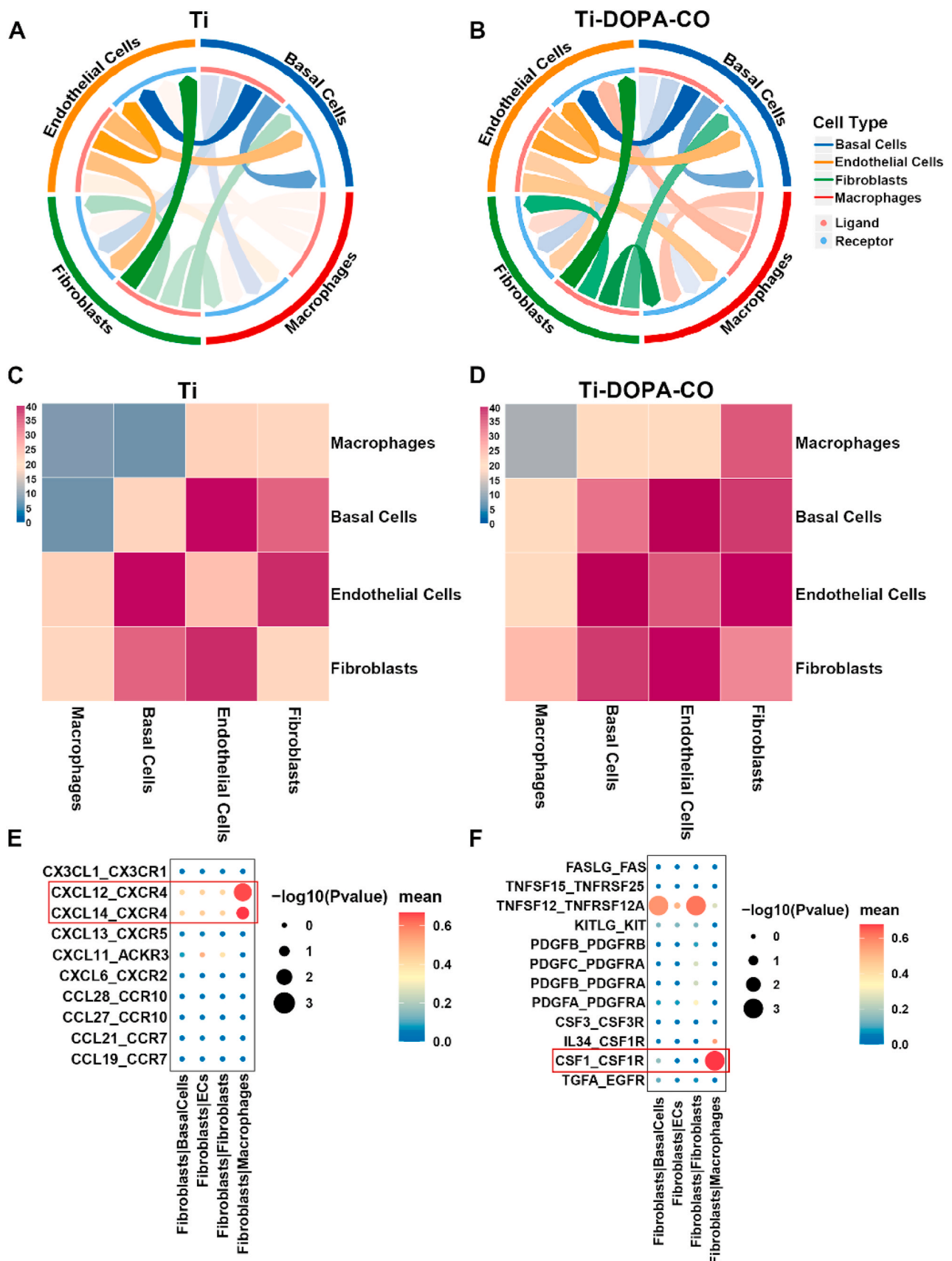


Fig. 9. Fibroblast-macrophage communication in the peri-implant microenvironment of Ti-DOPA-CO. A, B) Cellular communication network in Ti and Ti-DOPA-CO groups. Colors and width of edges represents number of interaction pairs between cell types. C, D) Heat map showing the overview of cellular communication in Ti and Ti-DOPA-CO groups. E, F) Dot plot showing the cellular interaction of ligand-receptor pair in different cell types of Ti-DOPA-CO group.

### 3. Conclusions

In this study, a smart titanium implant coating for enhanced soft tissue integration through CO-mediated immunomodulation and anti-biosis was developed. Upon NIR irradiation, the coating induces mild hyperthermia that triggers an on-demand release of CO, significantly increasing bactericidal efficacy within susceptible environments. Crucially, in the absence of NIR, the slow release of CO promotes macrophage polarization, shifting from a pro-inflammatory phenotype to a pro-regenerative phenotype. In a rat implantation model with induced infection, our designed surface effectively managed the bacterial infection, alleviated associated inflammation, and modulated immune microenvironment, leading to improved STI. Additionally, the immunoregulatory effects of the coating on the peri-implant microenvironment was also analyzed. The coating modulated the cytokine expression profile and fostered communication between macrophages and fibroblasts through the CXCL12/CXCL14/CXCR4 and CSF1-CSF1R ligand-receptor pair. We assert that the designed coating constitutes not merely a technical advance but also a conceptual shift for the development of implant surface in the STI enhancement.

### 4. Ethics approval and consent to participate

All the animal experimental procedures were conducted in accordance with institutional guidelines for the care and use of laboratory animals and protocols, which were approved by the Institutional Animal Care and Use Committee, Fourth Military Medical University (Approval No. 2023-kq-019).

### CRediT authorship contribution statement

**Minghao Zhou:** Writing – original draft, Visualization, Data curation. **Gangfeng Li:** Writing – review & editing, Methodology. **Jingwei Yu:** Writing – review & editing, Data curation. **Qian Zhou:** Validation, Methodology. **Kun Wang:** Methodology, Formal analysis. **Jiixin Kang:** Writing – review & editing, Validation. **Tengjiao Wang:** Project administration, Investigation, Funding acquisition, Conceptualization. **Peng Li:** Project administration, Funding acquisition. **Hongbo Wei:** Writing – review & editing, Validation, Supervision, Project administration, Funding acquisition.

### Declaration of competing interest

The authors declare the following financial interests/personal relationships which may be considered as potential competing interests: Peng Li reports financial support was provided by National Natural Science Foundation of China. Tengjiao Wang, Hongbo Wei reports financial support was provided by the Key Research and Development Program of Shaanxi. Peng Li reports financial support was provided by Shaanxi Provincial Science Fund for Distinguished Young Scholars. Tengjiao Wang reports financial support was provided by the Natural Science Foundation of Chongqing. If there are other authors, they declare that they have no known competing financial interests or personal relationships that could have appeared to influence the work reported in this paper.

### Acknowledgements

The authors acknowledge the financial support from the Natural Science Foundation of China (52073224 and 52073230), the Shaanxi Provincial Science Fund for Distinguished Young Scholars (2023-JC-JQ-32), Key Research and Development Program of Shaanxi (2024SF-YBXM-438 and 2022SF-165), and Natural Science Foundation of Chongqing (CSTB2023NSCQ-MSX0225).

### Appendix A. Supplementary data

Supplementary data to this article can be found online at <https://doi.org/10.1016/j.bioactmat.2024.06.010>.

### References

- [1] T. Guo, K. Gulati, H. Arora, P. Han, B. Fournier, S. Ivanovski, Orchestrating soft tissue integration at the transmucosal region of titanium implants, *Acta Biomater.* 124 (2021) 33–49, <https://doi.org/10.1016/j.actbio.2021.01.001>.
- [2] W.-r. Wang, J. Li, J.-t. Gu, B.-w. Hu, W. Qin, Y.-n. Zhu, Z.-x. Guo, Y.-X. Ma, F. Tay, K. Jiao, L. Niu, Optimization of lactoferrin-derived amyloid coating for enhancing soft tissue seal and antibacterial activity of titanium implants, *Adv. Healthcare Mater.* 12 (11) (2023) 2203086, <https://doi.org/10.1002/adhm.202203086>.
- [3] T. Guo, K. Gulati, H. Arora, P. Han, B. Fournier, S. Ivanovski, Race to invade: understanding soft tissue integration at the transmucosal region of titanium dental implants, *Dent. Mater.* 37 (5) (2021) 816–831, <https://doi.org/10.1016/j.dental.2021.02.005>.
- [4] S. Ivanovski, R. Lee, Comparison of peri-implant and periodontal marginal soft tissues in health and disease, *Periodontol* 76 (1) (2000) 116–130, <https://doi.org/10.1111/prd.12150>, 2018.
- [5] D.R. Dixon, R.M. London, Restorative design and associated risks for peri-implant diseases, *Periodontol* 81 (1) (2000) 167–178, <https://doi.org/10.1111/prd.12290>, 2019.
- [6] I.J. Kruyt, M.R.W. Bours, M.M. Rovers, M.K.S. Hol, J. Rongen, Economic evaluation of percutaneous titanium implants for bone conduction hearing: a cost-benefit analysis, *Otol. Neurotol.* 41 (5) (2020) 580–588, <https://doi.org/10.1097/mao.0000000000002616>.
- [7] A. Vilaça, R.M.A. Domingues, H. Tiainen, B.B. Mendes, A. Barrantes, R.L. Reis, M. E. Gomes, M. Gomez-Florit, Multifunctional surfaces for improving soft tissue integration, *Adv. Healthcare Mater.* 10 (8) (2021) 2001985, <https://doi.org/10.1002/adhm.202001985>.
- [8] T. Bjarnsholt, M. Whiteley, K.P. Rumbaugh, P.S. Stewart, P.Ø. Jensen, N. Fridmott-Møller, The importance of understanding the infectious microenvironment, *Lancet Infect. Dis.* 22 (3) (2022) e88–e92, [https://doi.org/10.1016/S1473-3099\(21\)00122-5](https://doi.org/10.1016/S1473-3099(21)00122-5).
- [9] P. Huang, J. Xu, L. Xie, G. Gao, S. Chen, Z. Gong, X. Lao, Z. Shan, J. Shi, Z. Zhou, Z. Chen, Y. Cao, Y. Wang, Z. Chen, Improving hard metal implant and soft tissue integration by modulating the “inflammatory-fibrous complex” response, *Bioact. Mater.* 20 (2023) 42–52, <https://doi.org/10.1016/j.bioactmat.2022.05.013>.
- [10] A. Shapouri-Moghaddam, S. Mohammadian, H. Vazini, M. Taghadosi, S.-A. Esmaili, F. Mardani, B. Seifi, A. Mohammadi, J.T. Afshari, A. Sahebkar, Macrophage plasticity, polarization, and function in health and disease, *J. Cell. Physiol.* 233 (9) (2018) 6425–6440, <https://doi.org/10.1002/jcp.26429>.
- [11] P.J. Murray, Macrophage polarization, *Annu. Rev. Physiol.* 79 (1) (2017) 541–566, <https://doi.org/10.1146/annurev-physiol-022516-034339>.
- [12] R. Liu, S. Chen, P. Huang, G. Liu, P. Luo, Z. Li, Y. Xiao, Z. Chen, Z. Chen, Immunomodulation-based strategy for improving soft tissue and metal implant integration and its implications in the development of metal soft tissue materials, *Adv. Funct. Mater.* 30 (21) (2020) 1910672, <https://doi.org/10.1002/adfm.201910672>.
- [13] J.R. Yu, M. Janssen, B.J. Liang, H.-C. Huang, J.P. Fisher, A liposome/gelatin methacrylate nanocomposite hydrogel system for delivery of stromal cell-derived factor-1 $\alpha$  and stimulation of cell migration, *Acta Biomater.* 108 (2020) 67–76, <https://doi.org/10.1016/j.actbio.2020.03.015>.
- [14] D.P. Vasconcelos, M. Costa, I.F. Amaral, M.A. Barbosa, A.P. Águas, J.N. Barbosa, Modulation of the inflammatory response to chitosan through M2 macrophage polarization using pro-resolution mediators, *Biomaterials* 37 (2015) 116–123, <https://doi.org/10.1016/j.biomaterials.2014.10.035>.
- [15] H. Wang, R. Huang, L. Bai, Y. Cai, M. Lei, C. Bao, S. Lin, S. Ji, C. Liu, X. Qu, Extracellular matrix-mimetic immunomodulatory hydrogel for accelerating wound healing, *Adv. Healthcare Mater.* 12 (27) (2023) 2301264, <https://doi.org/10.1002/adhm.202301264>.
- [16] B. Saleh, H.K. Dhaliwal, R. Portillo-Lara, E. Shirzaei Sani, R. Abdi, M.M. Amiji, N. Annabi, Local immunomodulation using an adhesive hydrogel loaded with mirna-laden nanoparticles promotes wound healing, *Small* 15 (36) (2019) 1902232, <https://doi.org/10.1002/sml.201902232>.
- [17] S.A. Ballestas, T.C. Turner, A. Kamalakar, Y.C. Stephenson, N.J. Willett, S. L. Goudy, E.A. Botchwey, Improving hard palate wound healing using immune modulatory autotherapies, *Acta Biomater.* 91 (2019) 209–219, <https://doi.org/10.1016/j.actbio.2019.04.052>.
- [18] M. Kharaziha, A. Baidya, N. Annabi, Rational design of immunomodulatory hydrogels for chronic wound healing, *Adv. Mater.* 33 (39) (2021) 2100176, <https://doi.org/10.1002/adma.202100176>.
- [19] S.-B. Wang, C. Zhang, J.-J. Ye, M.-Z. Zou, C.-J. Liu, X.-Z. Zhang, Near-infrared light responsive nanoreactor for simultaneous tumor photothermal therapy and Carbon monoxide-mediated anti-inflammation, *ACS Cent. Sci.* 6 (4) (2020) 555–565, <https://doi.org/10.1021/acscentsci.9b01342>.
- [20] K. Magierowska, T. Brzozowski, M. Magierowski, Emerging role of Carbon monoxide in regulation of cellular pathways and in the maintenance of gastric mucosal integrity, *Pharmacol. Res.* 129 (2018) 56–64, <https://doi.org/10.1016/j.phrs.2018.01.008>.
- [21] X. Zhang, Z. Yuan, J. Wu, Y. He, G. Lu, D. Zhang, Y. Zhao, R. Wu, Y. Lv, K. Cai, S. He, An orally-administered nanotherapeutics with Carbon monoxide supplying

- for inflammatory bowel disease therapy by scavenging oxidative stress and restoring gut immune homeostasis, *ACS Nano* 17 (21) (2023) 21116–21133, <https://doi.org/10.1021/acsnano.3c04819>.
- [22] H.-I. Choi, A. Zeb, M.-S. Kim, I. Rana, N. Khan, O.S. Qureshi, C.-W. Lim, J.-S. Park, Z. Gao, H.-J. Maeng, J.-K. Kim, Controlled therapeutic delivery of Co from Carbon monoxide-releasing molecules (corms), *J. Contr. Release* 350 (2022) 652–667, <https://doi.org/10.1016/j.jconrel.2022.08.055>.
- [23] K. Ling, F. Men, W.-C. Wang, Y.-Q. Zhou, H.-W. Zhang, D.-W. Ye, Carbon monoxide and its controlled release: therapeutic application, detection, and development of Carbon monoxide releasing molecules (corms), *J. Med. Chem.* 61 (7) (2018) 2611–2635, <https://doi.org/10.1021/acs.jmedchem.6b01153>.
- [24] W. Ma, X. Chen, L. Fu, J. Zhu, M. Fan, J. Chen, C. Yang, G. Yang, L. Wu, G. Mao, X. Yang, X. Mou, Z. Gu, X. Cai, Ultra-efficient antibacterial system based on photodynamic therapy and Co gas therapy for synergistic antibacterial and ablation biofilms, *ACS Appl. Mater. Interfaces* 12 (20) (2020) 22479–22491, <https://doi.org/10.1021/acsami.0c01967>.
- [25] L. Gao, J. Cheng, Z. Shen, G. Zhang, S. Liu, J. Hu, Orchestrating nitric oxide and Carbon monoxide signaling molecules for synergistic treatment of mrsa infections, *Angew. Chem. Int. Ed.* 61 (3) (2022) e202112782, <https://doi.org/10.1002/anie.202112782>.
- [26] K. Deepankumar, Q. Guo, H. Mohanram, J. Lim, Y. Mu, K. Pervushin, J. Yu, A. Miserez, Liquid-liquid phase separation of the green mussel adhesive protein pvpf-5 is regulated by the post-translated dopa amino acid, *Adv. Mater.* 34 (25) (2022) 2103828, <https://doi.org/10.1002/adma.202103828>.
- [27] S.J. Ma, E.M. Ford, L.A. Sawicki, B.P. Sutherland, N.I. Halaszynski, B.J. Carberry, N.J. Wagner, A.M. Kloxin, C.J. Kloxin, Surface chemical functionalization of wrinkled thiol-ene elastomers for promoting cellular alignment, *ACS Appl. Bio Mater.* 3 (6) (2020) 3731–3740, <https://doi.org/10.1021/acsabm.0c00346>.
- [28] S.-H. Yoon, M.R.K. Mofrad, Cell adhesion and detachment on gold surfaces modified with a thiol-functionalized rgd peptide, *Biomaterials* 32 (30) (2011) 7286–7296, <https://doi.org/10.1016/j.biomaterials.2011.05.077>.
- [29] H.-Y. Sun, C.-Y. Fang, T.-J. Lin, Y.-C. Chen, C.-Y. Lin, H.-Y. Ho, M.H.-C. Chen, J. Yu, D.-J. Lee, C.-H. Chang, H.-Y. Chen, Thiol-reactive polylenes as a robust coating for biomedical materials, *Adv. Mater. Interfac.* 1 (6) (2014) 1400093, <https://doi.org/10.1002/admi.201400093>.
- [30] J. Tomastik, R. Ctvrtlik, Nanoscratch test — a tool for evaluation of cohesive and adhesive properties of thin films and coatings, *EPJ Web Conf.* 48 (2013) 00027, doi: 10.1051/epjconf/20134800027.
- [31] G. Mallikarjunachari, P. Ghosh, Analysis of strength and response of polymer nano thin film interfaces applying nanoindentation and nanoscratch techniques, *Polymer* 90 (4) (2016) 53–66, <https://doi.org/10.1016/j.polymer.2016.02.042>.
- [32] J.A. Lenis, P. Rico, J.L.G. Ribelles, M.A. Pacha-Olivenza, M.L. González-Martín, F. J. Bolívar, Structure, morphology, adhesion and in vitro biological evaluation of antibacterial multi-layer ha-Ag/SiO<sub>2</sub>/TiN/Ti coatings obtained by Rf magnetron sputtering for biomedical applications, *Mater. Sci. Eng. C* 116 (2020) 111268, <https://doi.org/10.1016/j.msec.2020.111268>.
- [33] J.L. Roti Rotti, Cellular responses to hyperthermia (40–46°C): cell killing and molecular events, *Int. J. Hyperther.* 24 (1) (2008) 3–15, <https://doi.org/10.1080/02656730701769841>.
- [34] R. Chen, C. Zhao, Z. Chen, X. Shi, H. Zhu, Q. Bu, L. Wang, C. Wang, H. He, A bionic cellulose nanofiber-based nanocage wound dressing for nir-triggered multiple synergistic therapy of tumors and infected wounds, *Biomaterials* 281 (2022) 121330, <https://doi.org/10.1016/j.biomaterials.2021.121330>.
- [35] Z. He, Y. Gao, H. Zhang, Y. Xue, F. Meng, L. Luo, Mitochondrion-anchored photosensitizer with near infrared-I aggregation-induced emission for near infrared-ii two-photon photodynamic therapy, *Adv. Healthcare Mater.* 10 (24) (2021) 2101056, <https://doi.org/10.1002/adhm.202101056>.
- [36] H. Chu, J. Zhao, Y. Mi, Z. Di, L. Li, Nir-light-mediated spatially selective triggering of anti-tumor immunity via upconversion nanoparticle-based immunodevices, *Nat. Commun.* 10 (1) (2019) 2839, <https://doi.org/10.1038/s41467-019-10847-0>.
- [37] S. Zhu, B. Zhao, M. Li, H. Wang, J. Zhu, Q. Li, H. Gao, Q. Feng, X. Cao, Microenvironment responsive nanocomposite hydrogel with nir photothermal therapy, vascularization and anti-inflammation for diabetic infected wound healing, *Bioact. Mater.* 26 (2023) 306–320, <https://doi.org/10.1016/j.bioactmat.2023.03.005>.
- [38] X. Yao, P. Yang, Z. Jin, Q. Jiang, R. Guo, R. Xie, Q. He, W. Yang, Multifunctional nanoplatfor for photoacoustic imaging-guided combined therapy enhanced by Co induced ferroptosis, *Biomaterials* 197 (2019) 268–283, <https://doi.org/10.1016/j.biomaterials.2019.01.026>.
- [39] W. Feng, D. Liu, S. Feng, G. Feng, Readily available fluorescent probe for Carbon monoxide imaging in living cells, *Anal. Chem.* 88 (21) (2016) 10648–10653, <https://doi.org/10.1021/acs.analchem.6b03073>.
- [40] B. Galy, M. Conrad, M. Muckenthaler, Mechanisms controlling cellular and systemic iron homeostasis, *Nat. Rev. Mol. Cell Biol.* 25 (2) (2024) 133–155, <https://doi.org/10.1038/s41580-023-00648-1>.
- [41] D. Wu, X. Chang, J. Tian, L. Kang, Y. Wu, J. Liu, X. Wu, Y. Huang, B. Gao, H. Wang, G. Qiu, Z. Wu, Bone mesenchymal stem cells stimulation by magnetic nanoparticles and a static magnetic field: release of exosomal mir-1260a improves osteogenesis and angiogenesis, *J. Nanobiotechnol.* 19 (1) (2021) 209, <https://doi.org/10.1186/s12951-021-00958-6>.
- [42] K. Yang, X. Zhou, Z. Li, Z. Wang, Y. Luo, L. Deng, He, D. Ultrastretchable, self-healable, and tissue-adhesive hydrogel dressings involving nanoscale tannic acid/ferric ion complexes for combating bacterial infection and promoting wound healing, *ACS Appl. Mater. Interfaces* 14 (38) (2022) 43010–43025, <https://doi.org/10.1021/acsami.2c13283>.
- [43] N. Xu, Y. Gao, Z. Li, Y. Chen, M. Liu, J. Jia, R. Zeng, G. Luo, J. Li, Y. Yu, Immunoregulatory hydrogel decorated with tannic acid/ferric ion accelerates diabetic wound healing via regulating macrophage polarization, *Chem. Eng. J.* 466 (15) (2023) 143173, <https://doi.org/10.1016/j.cej.2023.143173>.
- [44] Z. Chen, W. Zhang, M. Wang, L.J. Backman, J. Chen, Effects of zinc, magnesium, and iron ions on bone tissue engineering, *ACS Biomater. Sci. Eng.* 8 (6) (2022) 2321–2335, <https://doi.org/10.1021/acsbiomaterials.2c00368>.
- [45] C.R. Arciola, D. Campoccia, P. Speziale, L. Montanaro, J.W. Costerton, Biofilm Formation in Staphylococcus implant infections. A review of molecular mechanisms and implications for biofilm-resistant materials, *Biomaterials* 33 (26) (2012) 5967–5982, <https://doi.org/10.1016/j.biomaterials.2012.05.031>.
- [46] L.J.A. Heitz-Mayfield, N.P. Lang, Comparative biology of chronic and aggressive periodontitis vs. Peri-implantitis, *Periodontol* 53 (1) (2000) 167–181, <https://doi.org/10.1111/j.1600-0757.2010.00348.x>.
- [47] H.M. Southam, M.P. Williamson, J.A. Chapman, R.L. Lyon, C.R. Trevitt, P.J. F. Henderson, R.K. Poole, Carbon-Monoxide-Releasing molecule-2 (Corm-2) is a misnomer: ruthenium toxicity, not Co release, accounts for its antimicrobial effects, *Antioxidants* 10 (6) (2021) 915, <https://doi.org/10.3390/antiox10060915>.
- [48] L.K. Wareham, R.K. Poole, M. Tinajero-Trejo, CO-releasing metal carbonyl compounds as antimicrobial agents in the post-antibiotic era, *J. Biol. Chem.* 290 (31) (2015) 18999–19007, <https://doi.org/10.1074/jbc.R115.642926>.
- [49] X. Gao, L. Yan, W. Zhang, Y. Lv, P. Ou, R. Hang, A. Gao, L. Tong, P.K. Chu, H. Wang, Dual-switched Carbon monoxide nano gas tank for auto-diagnosis and precision therapy of osteoarthritis, *Nano Today* 53 (2023) 102047, <https://doi.org/10.1016/j.nantod.2023.102047>.
- [50] Z. Jin, Y. Wen, L. Xiong, T. Yang, P. Zhao, L. Tan, T. Wang, Z. Qian, B.-L. Su, Q. He, Intratumoral H<sub>2</sub>O<sub>2</sub>-triggered release of Co from a metal carbonyl-based nanomedicine for efficient Co therapy, *Chem. Commun.* 53 (40) (2017) 5557–5560, <https://doi.org/10.1039/C7CC01576C>.
- [51] J.A. Lemire, J.J. Harrison, R.J. Turner, Antimicrobial activity of metals: mechanisms, molecular targets and applications, *Nat. Rev. Microbiol.* 11 (6) (2013) 371–384, <https://doi.org/10.1038/nrmicro3028>.
- [52] R. Ma, L. Fang, L. Chen, X. Wang, J. Jiang, L. Gao, Ferroptotic stress promotes macrophages against intracellular bacteria, *Theranostics* 12 (5) (2022) 2266–2289, <https://doi.org/10.7150/thno.66663>. Research Paper.
- [53] M.-N. Abdallah, Z. Badran, O. Ciobanu, N. Hamdan, F. Tamimi, Strategies for optimizing the soft tissue seal around osseointegrated implants, *Adv. Healthcare Mater.* 6 (20) (2017) 1700549, <https://doi.org/10.1002/adhm.201700549>.
- [54] G. Yang, M. Fan, J. Zhu, C. Ling, L. Wu, X. Zhang, M. Zhang, J. Li, Q. Yao, Z. Gu, X. Cai, A multifunctional anti-inflammatory drug that can specifically target activated macrophages, massively deplete intracellular H<sub>2</sub>O<sub>2</sub>, and produce large amounts Co for a highly efficient treatment of osteoarthritis, *Biomaterials* 255 (2020) 120155, <https://doi.org/10.1016/j.biomaterials.2020.120155>.
- [55] Z. Yuan, J. Wu, Y. Xiao, H. Yang, S. Meng, L. Dai, P. Li, K. Cai, A photo-therapeutic nanocomposite with bio-responsive oxygen self-supplying combats biofilm infections and inflammation from drug-resistant bacteria, *Adv. Funct. Mater.* 33 (37) (2023) 2302908, <https://doi.org/10.1002/adfm.202302908>.
- [56] Z. Yuan, J. Wu, Z. Fu, S. Meng, L. Dai, K. Cai, Polydopamine-mediated interfacial functionalization of implants for accelerating infected bone repair through light-activatable antibiosis and Carbon monoxide gas regulated macrophage polarization, *Adv. Funct. Mater.* 32 (27) (2022) 2200374, <https://doi.org/10.1002/adfm.202200374>.
- [57] Z. Yuan, C. Lin, L. Dai, Y. He, J. Hu, K. Xu, B. Tao, P. Liu, K. Cai, Near-infrared light-activatable dual-action nanoparticle combats the established biofilms of methicillin-resistant Staphylococcus aureus and its accompanying inflammation, *Small* 17 (13) (2021) 2007522, <https://doi.org/10.1002/smll.202007522>.
- [58] M. Ruopp, S. Reiländer, D. Haas, I. Caruana, D. Kronenberg, W. Schmehl, R. Stange, L. Meinel, Transdermal Carbon monoxide delivery, *J. Contr. Release* 357 (2023) 299–308, <https://doi.org/10.1016/j.jconrel.2023.03.034>.
- [59] Y. Zeng, M. Fan, Q. Zhou, D. Chen, T. Jin, Z. Mu, L. Li, J. Chen, D. Qiu, Y. Zhang, Y. Pan, X. Shen, X. Cai, Reactive oxygen species-activated Co versatile nanomedicine with innate gut immune and microbiome remodeling effects for treating inflammatory bowel disease, *Adv. Funct. Mater.* 33 (49) (2023) 2304381, <https://doi.org/10.1002/adfm.202304381>.
- [60] X. Cai, R. Chen, K. Ma, F. Wang, Y. Zhou, Y. Wang, T. Jiang, Identification of the cxcl12-cxcr4/cxcr7 Axis as a potential therapeutic target for immunomodulating macrophage polarization and foreign body response to implanted biomaterials, *Appl. Mater. Today* 18 (2020) 100454, <https://doi.org/10.1016/j.apmt.2019.100454>.
- [61] M.B. Buechler, W. Fu, S.J. Turley, Fibroblast-macrophage reciprocal interactions in health, fibrosis, and cancer, *Immunity* 54 (5) (2021) 903–915, <https://doi.org/10.1016/j.immuni.2021.04.021>.